3

Application of Empirical Green's Functions in Earthquake Source, Wave Propagation and Strong Ground Motion Studies

Lawrence Hutchings and Gisela Viegas
Lawrence Berkeley National Laboratory
USA

1. Introduction

Over the last couple of decades, empirical Green's functions [EGFs] have been increasingly used in earthquake source studies, crustal attenuation studies, strong ground-motion prediction, finite rupture modeling, and site-response studies. Theoretically, Green's functions are the impulse response of the medium, and EGFs are recordings used to provide this impulse response. In this chapter, we review the theoretical and observational basis for identifying and using small earthquakes as empirical Green's functions—and their application. We generally refer to analyses that use EGFs as "the EGF method". The seismic record of an earthquake contains information on the earthquake source, the path the seismic waves propagated through, the site response of the geology beneath the recording site, and the response of the instrument that recorded the ground motion. In seismology, we are interested in isolating either source, path, or site information, depending on the study focus. The instrument response is usually known and easy to remove from recordings, but the same is not true for the other factors. Seismic waves propagate in the earth in a complex way. They are reflected and refracted at interfaces between rocks with different properties, attenuated throughout the path between the earthquake source and the station by scattering and anelastic effects, subjected to energy focusing and defocussing due to lateral changes in the refractive properties of the rock, and amplified and highly attenuated near the recording station as waves pass through unconsolidated near-surface material.

These propagation complexities are not well captured by crustal models, which provide the basis for calculating Green's functions, especially for high frequencies (> 1 Hz). At higher frequencies, wave propagation is very sensitive to small crustal heterogeneities, which are generally not well known; at low frequencies (< 1 Hz), wave propagation can be modeled fairly accurately. EGFs can be used instead of mathematical calculations to more accurately represent seismic wave propagation in the geologically heterogeneous crust. The EGF method is the best available method because it empirically corrects for unknown path and site effects, for which a short wavelength resolution is needed. However, true EGFs contain the source rupture process of the small earthquakes in the recorded seismograms. No earthquake has a true impulsive source. Therefore, one must be careful using EGFs.

There has not been uniformity in defining EGF's. Recordings of earthquakes with magnitudes less than 1.0 to 7.0 have been used as EGFs. Here, we apply a strict

mathematical definition to EGFs and discuss different uses of EGFs with respect to this definition. We define EGFs as recordings of sources that satisfy impulsive-point dislocation criteria within the frequency band the EGFs are used. The word "satisfy" is included in the definition of EGFs because there is no true impulsive point source in nature. Therefore, the definition of an EGF can be dependent upon the frequency range of interest. Sources in nature may be explosions, rock bursts, earthquakes, or any impulsive source. Under certain constraints, EGFs can be used as point sources. The impulsive point source definition is consistent with the mathematical definition of an elastodynamic Green's function, which is the response at a particular location to a uni-directional, unit-impulsive, point source at another location.

EGFs were initially used in attenuation and earthquake-source studies (e.g., Bakun and Bufe, 1975, and references within). Bakun and Bufe noted that for small earthquakes (<M4), for which corner frequencies are within the frequency band most affected by attenuation and site effects, deconvolution could isolate source and propagation-path effects. Initially, the method was applied in the frequency domain by a spectral ratio method. The underlying reasoning for doing this was that common station recordings of closely located earthquakes shared the same propagation path and could be used to form "ratios of spectra," and thus "cancel the common propagation path effects" (Bakum and Bufe, 1975).

Subsequent studies further developed EGF methods. Frankel (1982), Mueller (1985), Hough et al., (1991), Abercrombie and Rice (2005), and Viegas et al. (2010) performed analysis of EGFs in the frequency domain to obtain source parameters of larger earthquakes and attenuation prosperities of the medium. Frankel and Kanamori (1983), Frankel et al. (1986), Mori and Frankel (1990), Mori et al. (2003) performed similar analysis in the time domain. Hough (1997), Hough et al. (1999), Prejean and Ellsworth (2001), Ide et al. (2003), Prieto et al. (2004), Shearer et al. (2006) analyzed multiple earthquakes simultaneously to obtain source properties and kappa (near site attenuation). Mayeda et al. (2007) and Viegas (2009) used source spectra derived from coda waves instead of direct waves to obtain source properities.

Hartzell (1978) and Wu (1978) first suggested using EGFs to calculate strong ground motion. Using small earthquakes to provide EGF's for synthesizing larger earthquakes is very practical; small earthquakes occur hundreds of times more frequently than larger earthquakes and EGFs can be readily obtained in a short period of time before a large earthquake occurs. Hartzell and Wu suggested using EGFs as the Green's function in the representation relation along with synthetic rupture processes for calculating (synthesizing) the resulting ground motion. That is, the fault of the large earthquake is represented as a summation of subfaults, or elemental point sources, for which EGFs are available. Figure 1 dramatizes the wave propagation effects that occur from different portions of a fault, so that as an earthquake ruptures, EGFs account for the different travel paths through the heterogeneous geology. Hutchings (1991) and Hartzell et al. (1999) designed particular rupture models to represent what actual earthquake might do. This followed Boatwright (1981), who designed quasi-dynamic sources. Guatteri et al. (2003) further developed source modeling by including actual dynamic rupture process in the calculations. Irikura (1984) used a relatively large earthquake as an EGF and modified it to represent the strong ground motion from an even larger earthquake (usually 1 or 2 magnitude units higher). In this approach the EGF was not isolated as an impulsive point source, and the larger earthquake was made up of fairly large sub-events. Joyner and Boore (1986) examined the statistics of how to add up sub-events to create a larger earthquake. Frankel (1991) proposed a fractal summation of scaled EGFs to represent the source process as a statistical process. Tumarkin (1994) and Abrahamson and

Bolt (1997) modified recordings of relatively large earthquakes to fit a target spectra of an even larger earthquake. Somerville et al. (1991) used the recordings near a large earthquake as an empirical source function and calculated the wave propagation effects. All these source models have different implications for the synthesis process, and are discussed below. We also examine validation procedures to verify the usefulness of methods.

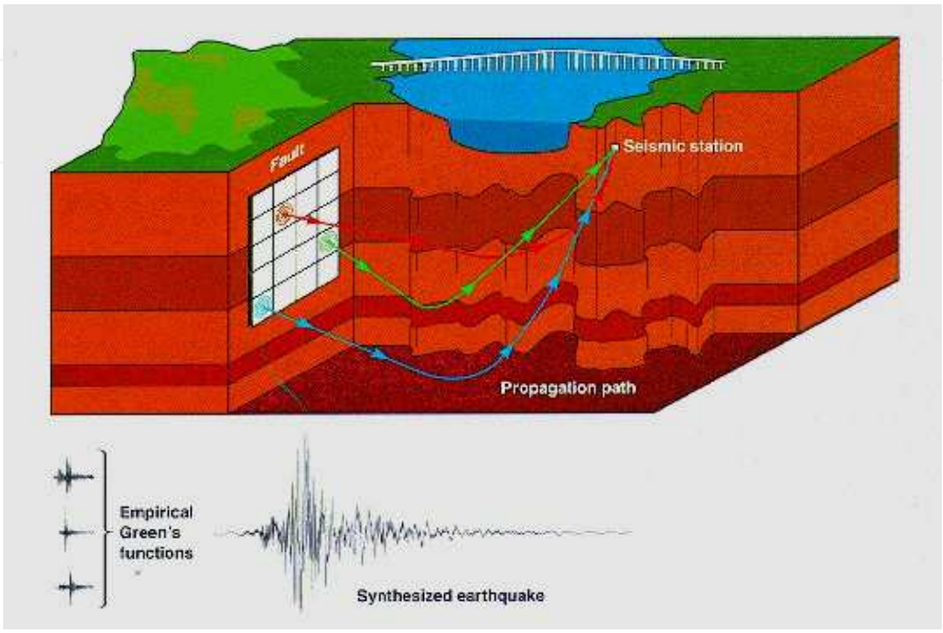

Fig. 1. Illustration of wave propagation effects that occur from different portions of a fault as an earthquake ruptures. Each EGF accounts for a different travel path through the heterogeneous geology.

There are several limitations to EGFs. The selection of an EGF for use in source studies follows strict criteria that are not always possible to fulfill. Thus, a suitable EGF function may not be available, limiting the number of earthquakes that can be analyzed. The bandwidth of the EGF for which enough signal above noise is available is another limiting factor in source studies. For very small EGF earthquakes or noisy surface stations, the available bandwidth may not be enough to perform the source analysis, even though there is sufficient signal from the earthquake being analyzed. Limited instrument bandwidth, another potentially serious limitation, may bias the source parameters. However, the EGF method profits from having a good distribution of recording stations, providing a good azimuthal coverage so that source directivity effects may be accounted for.
There are also a number of limitations in applying EGF methods to ground-motion modeling:

1. In virtually all practical applications, there are insufficient number of EGFs to provide an impulse response for all portions of a fault rupture to be modeled.
2. EGFs cannot accurately model variations in focal mechanism solutions.
3. Noise levels in recordings limit their usable frequency band (usually between 0.2 Hz to 25.0 Hz or narrower in seismically active regions such as the Western U.S).
4. A distribution of stations with good azimuthal coverage is necessary to ascertain the locations and source parameters of the small earthquakes that would provide EGFs.

5. Good-quality recordings of seismograms have to be captured at the locations of interest for ground-motion synthesis.

In this chapter, we describe the theoretical and observational basis for identifying and using small earthquakes as EGFs and review some of the typically used methods in earthquake source and strong-ground-motion studies. We also discuss the advances in the scientific knowledge of earthquake sources made possible by EGFs. Finally, we discuss using the application of the EGF method (in strong-ground-motion prediction) to probabilistic seismic-hazard analysis.

2. Theoretical considerations

The representation relation (Aki and Richards, 2002) is the fundamental, elastodynamic, mathematical description of an earthquake and the resulting ground motion. It is expressed as

$$u_n(X,t) = \int_A m_{pq}(X',t') * G_{np,q}(X',t';X,t)dA\,, \tag{1}$$

where u_n is the ground displacement in the direction $\hat{x}_n$, at location X and time t, resulting from the integral over the fault surface of the convolution of the source function $m_{pq}(X',t')$ with the derivative of the Green's function tensor $G_{np}(X',t';X,t)$, with respect to the $\hat{x}_q$ direction, at location X' and time t' on the source; $*$ is the convolution operator, and A is the fault surface. The Green's function tensor is the contribution to the displacement in the $\hat{x}_n$ direction from a unidirectional unit-impulse in direction $\hat{x}_p$. A complete description of Equation (1) can be found in Aki and Richards (2002, Chapter 3), whose notation we follow. Every EGF synthesis approach utilizes this representation relation. The differences between methods are in how the equation is solved, what the source function is, and what is used for the Green's functions.

The source function is defined as the moment density tensor m_{pq},

$$m_{pq}(X',t') = \left[s_i(X',t')\right]\hat{n}_j(X')c_{ijpq}\,, \tag{2}$$

which is the strength of the double couple with dimensions of moment per unit area. Here, $\hat{n}$ is the unit normal vector to the fault in source coordinates, and $s(X',t')$ is the source-time function. The source-time function $s_i(X',t')$ specifies the spatial and time distribution of slip along the fault in the $\hat{x}_i$ direction. [ ] symbolizes directional displacement between two sides of the fault. c_{ijpq} is the fourth-order elasticity tensor, which relates stress to strain.

For a fault surface embedded in a linearly elastic and isotropic body, and located many wavelengths away from the recording site, the moment density tensor m_{pq} is defined as

$$m_{pq}(X',t') = \lambda\,\hat{n}_k(X')\left[s_k(X',t')\right]\delta_{pq} + \mu\left\{\left[s_p(X',t')\right]\hat{n}_q(X') + \left[s_q(X',t')\right]\hat{n}_p(X')\right\}. \tag{3a}$$

Here, λ and μ are the Lamé constants at the source, and δ_{pq} is the Kronecker delta function (equal to 1 for p=q, equal to 0 for p≠q). Assuming that the fault slip is parallel to the fault surface, so that the product between the fault normal and the slip is zero, Equation (2) can be simplified to

$$m_{pq}(X^{'},t^{'}) = \mu\left\{\left[s_p(X^{'},t^{'})\right]\hat{n}_q(X^{'}) + \left[s_q(X^{'},t^{'})\right]\hat{n}_p(X^{'})\right\}. \quad (3b)$$

The source-time function can be described in scalar form if we assume that at each point along the fault, the slip function has the same time dependence in all directions (Johnson, 1975). Then, the moment density tensor can be simplified to

$$m_{pq}(X^{'},t^{'}) = \mu S(X^{'},t^{'})\left\{\hat{s}_p(X^{'})\hat{n}_q(X^{'}) + \hat{s}_q(X^{'})\hat{n}_p(X^{'})\right\}. \quad (4)$$

$S(X',t')$ is the scalar-source time function, and the symbol for differential slip is dropped. The term $(\hat{s}_p\hat{n}_q + \hat{s}_q\hat{n}_p)$ is the focal mechanism with slip in direction $\hat{s}$ and fault normal in direction $\hat{n}$. To express this relation for an arbitrary fault orientation requires general coordinates that describe the fault orientation. We use the convention of Aki and Richards (2002, page 109).

The impulsive point-source solution describes what we will call the EGF. For observed wavelengths much greater than the linear dimensions of the fault, the Green's functions are effectively in phase from all points along the fault and independent of the X' coordinates. This is the condition for a point source, and Equation (1) can then be written as

$$u_n(X,t) = \int_A m_{pq}(X^{'},t^{'})dA * G_{np,q}(X^{'},t^{'};X,t). \quad (5)$$

Substituting Equation (4) into Equation (5), we obtain

$$u_n(X,t) = \int_A \mu S(X^{'},t^{'})\left\{\hat{s}_p(X^{'})\hat{n}_q(X^{'}) + \hat{s}_q(X^{'})\hat{n}_p(X^{'})\right\}dA * G_{np,q}(X^{'},t^{'};X,t). \quad (6)$$

If the periods of observed waves are also much greater than the duration of faulting, the time dependence of the source cannot be observed, and the source-time function at the source $S(X',t')$ can be replaced by a unit Heaviside step function scaled by the average slip over the fault surface, $\bar{s}\cdot H(t^{'})$. In addition, replacing the integral over the fault surface by the total area A, and using e instead of u to describe the ground displacement associated of the EGF, Equation (6) can be rewritten as

$$e_n(X,t) = \mu A\bar{s}H(t^{'})(\hat{s}_p\hat{n}_q + \hat{s}_q\hat{n}_p) * G_{np,q}(X^{'},t^{'};X,t), \quad (7)$$

in which the focal mechanism solution is that of the overall fault displacement. Defining the seismic moment of the empirical Green's function as

$$M_0^e = \mu A\bar{s}, \quad (8)$$

and substituting it into Equation (7), the observed ground motion from a point, step-impulsive source-time function can be expressed in the formal notation of a Green's function as

$$e_n(X_0^{'},t_0^{'};X,t) = M_0^e(\hat{s}_p\hat{n}_q + \hat{s}_q\hat{n}_p)H(t^{'} - t_0^{'}) * G_{np,q}(X_0^{'},t_0^{'};X,t). \quad (9)$$

Here $e_n(X_0^{'},t_0^{'};X,t)$ is the solution for an EGF at position X and time t due to an impulsive-point dislocation source at the hypocenter $X_0^{'}$, and origin time $t_0^{'}$; and $H(t'-t_0')$ is the unit

step source-time function. Since a true point-source dislocation does not occur in nature, this equation only applies to recordings of earthquakes in frequencies below the source corner frequency. So, EGFs are recordings that essentially have impulsive point dislocation sources, i.e. in the frequency band of observation the spectra is flat and they cannot be distinguished from true impulsive point sources.

EGFs can be used to solve the representation relation exactly, under certain conditions. If we represent the fault area as a discrete summation of subfaults, the integral in Equation (6) can be replaced by a discrete sum over N elemental areas A_i such that ΣA_i equals the total rupture area,

$$u_n(X,t) = \sum_{i=1}^{N} \mu_i A_i S(t')_i (\hat{s}_p \hat{n}_q + \hat{s}_q \hat{n}_p)_i * G_{np,q}(X', t'; X, t)_i \ . \tag{10}$$

We can use the EGF analytical solution described by Equation (9) to provide the focal mechanism $(\hat{s}_p \hat{n}_q + \hat{s}_q \hat{n}_p)$ and the derivative of the elastodynamic Green's functions $G_{np,\,q}$ for each elemental area, and substitute it into Equation (10) to get

$$u_n(X,t) = \sum_{i=1}^{N} \frac{\mu_i A_i S'(t')_i}{M_{0\,i}^{e}} * e_n\left(X', t'; X, t\right)_i \ . \tag{11}$$

Here, the analytical solution for the slip function of the larger event, $S'(t')_i$ is the desired slip function for element i deconvolved by the EGF step function, $S'(t')_i = S(t') \otimes H(t' - t_0')_i$, where $\otimes$ represents deconvolution. Both large earthquakes and EGF earthquakes are assumed to share the same focal mechanism, so that the dislocation vectors have the same orientations, and the wave phases have the same polarity and relative amplitudes. $M_{0\,i}^{e}$ is the scalar seismic moment of the source event for the EGF, and $e_n(X,t)_i$ is the EGF for the i^{th} element obtained from recordings of small earthquakes with an effective step-source time function; u_n has the same units as e_n, and any differentiation with respect to t operates only on u_n and e_n. Each element can have a different recording as an EGF. EGFs are adjusted so that each has an origin time at the arrival of a rupture front. Because EGFs cannot be recorded from each point on the fault, they must be interpolated. (Interpolation schemes are not shown as part of Equation (11) and are discussed later in the chapter.) Unfortunately, it is not possible to decompose the EGF into a tensor component solution so that different focal-mechanism solutions could be used in Equation (9). Hutchings and Wu (1990) provide a detailed description of this problem, and we discuss its implications later in this chapter. If larger earthquakes are used to provide EGFs, then e_n has a source-time function that is not necessarily known. Then, the entire Equation (9) can be identified as the solution for the composite event, where $S'(t')_i$ is not known but part of the empirical recording.

An important form of the representation relation can be derived if the slip function is discretized into a series of step functions,

$$S(t') = \sum_{j=1}^{L} \bar{s} H(t' - \tau_j^s) \ , \tag{12}$$

where τ_j^s are phase delays due to the slip function, and their sum is the rise time. If the step function of the EGF is used, then the deconvolution with a step function as in Equation (11) is not necessary, and Equation (10) can be written as

$$u_n(X,t) = \sum_{i=1}^{N} \sum_{j=1}^{L} \frac{\mu_i A_i \bar{s}_{ij}}{M_{oi}^{\mathrm{e}}} e_n(X, t_i^{'} - \tau_i^r - \tau_j^s)_i \ , \tag{13}$$

where s_{ij} is calculated from the slip function and τ_i^r are phase delays due to rupture. To develop this relationship further and into a form often used in ground-motion synthesis, we combine time delays and summations into a single summation,

$$u_n(X,t) = \sum_{j=1}^{\eta} \kappa_j e_n(X, t_i^{'} - \tau_j)_j \ , \tag{14}$$

where, τ_j includes all time delays, and

$$\kappa_j = \frac{\mu_j A_j \bar{s}_j}{M_{oj}^e}, \text{ and } \eta = \sum_{i=1}^{N} L_i \ . \tag{15}$$

Equations (13) and (14) are often used as the form for composite earthquake ground-motion-synthesis models. In this approach, relatively large events are used as EGFs, with a large EGF source-time function employed as part of the source-time function of the larger event. Equation (14) would be expressed as

$$u_n(X,t) = \sum_{j=1}^{\eta} \kappa_j \left[\int_A m_{pq}(X^{'}, t^{'}) * G_{np,q}(X^{'}, t^{'}; X, t) dA \right]_j \ , \tag{16}$$

where Equation (1) describes the recording of a large event used as an EGF. Then, a solution with point sources would be

$$u_n(X,t) = \sum_{j=1}^{\eta} \kappa_j \sum_{l=1}^{\varsigma} \kappa_l e_n(X, t_i^{'} - \tau_l - \tau_j)_l \ . \tag{17}$$

To examine the Fourier amplitude spectra of synthesized earthquakes with EGFs, we can express the modulus of the power spectrum of Equation (14) as

$$\left| U(\omega)^2 \right| = \sum_{j=1}^{\eta} \kappa_j^2 E_j(\omega) E_j^*(\omega) + \sum_{j=1}^{\eta} \sum_{\substack{k=1 \\ \mathrm{j} \neq \mathrm{k}}}^{\eta} \kappa_j \kappa_k E_j(\omega) E_k^*(\omega) e^{-i\omega\tau_j} e^{i\omega\tau_k} \ . \tag{18}$$

$E(\omega)$ is the Fourier transform of the EGF and * indicates a complex conjugate. The phase spectrum defined by the rupture process is

$$\left| P(\omega) \right| = \sum_{j=1}^{\eta} \sum_{\substack{k=1 \\ j \neq k}}^{\eta} e^{-i\omega\tau_j} e^{i\omega\tau_k} \ . \tag{19}$$

A simple form of the Fourier amplitude spectrum can be developed if it is assumed that EGF Fourier amplitude spectra are similar at a particular recording site, even if their phase spectra can be quite different. Then, the Fourier amplitude spectrum of the synthesized seismogram can be expressed as

$$|U(\omega)| = |E(\omega)| \sqrt{\sum_{j=1}^{\eta} \kappa_j^2 + \sum_{j=1}^{\eta} \sum_{\substack{k=1 \\ j \neq k}}^{\eta} \kappa_j \kappa_k \cos(\varphi_j - \varphi_k + \omega\tau_k - \omega\tau_j)} \,, \tag{20}$$

where $\varphi(\omega)$ is the phase spectrum of the EGF.

Scaling effects and the effects of different rupture parameters on the Fourier amplitude spectra are fairly easy to observe. At low frequencies, $\omega \to 0$, the phase spectrum of different Green's functions is the same, and the spectral amplitudes are expressed as

$$|U(\omega)| = |E(\omega)| \frac{M_0}{M_0^e} \,. \tag{21}$$

Equation (21) is an expression for the largest spectral amplitudes possible for the synthesized seismograms. Spectra at higher frequencies are modulated by the phase effects of different EGFs and by the delay times caused by rupture velocity and the slip function (Equation 18). The summation of these modulated spectra gives the shape of the spectra at high frequencies. It is clear, then, that the frequency content of synthesized seismograms (and actual recordings as well) is dependent upon the constructive and destructive interference effects caused by the rupture parameters and spatial variation of the Green's functions. No scaling relation is needed to describe the large earthquake other than the sum of the moments of the elemental areas, which need to add up to that of the large earthquake.

Determining earthquake source parameters typically involves the deconvolution of the target earthquake with a single EGF earthquake. This assumes that the Green's function is the same for all points along the rupture of the larger event, so this approach works well only if both earthquakes are recorded in the far field. To successfully deconvolve the large earthquake by a single EGF earthquake, further constraints have to be introduced that guarantee the suitability of the EGF earthquake. Both earthquakes need to be recorded at the same station. The larger and smaller earthquakes have to be co-located so that the deconvolution process removes all propagation-path and recording-site effects from the records of the large event. There should be at least a one-magnitude difference between the two earthquakes, so that the EGF and larger-earthquake source effects are distinguishable. Then, from Equation (1), we have

$$\begin{aligned} u_n(X,t) \otimes e_n(X,t) &= \int_A m_{pq}^u(X',t') * G_{np,q}(X',t';X,t)dA \otimes \int_A m_{pq}^e(X',t') * G_{np,q}(X',t';X,t)dA \\ &= \left[\mu A^u \bar{s}^u d^u(t'-t_0')(\hat{s}_p\hat{n}_q + \hat{s}_q\hat{n}_p)_i * G_{np,q}(X',t';X,t) \right] \otimes \\ &\qquad \left[\mu A^e \bar{s}^e d^e(t'-t_0')(\hat{s}_p\hat{n}_q + \hat{s}_q\hat{n}_p)_i * G_{np,q}(X',t';X,t) \right] \\ &= M_0^u(\hat{s}_p\hat{n}_q + \hat{s}_q\hat{n}_p)d^u(t'-t_0') \otimes M_0^e(\hat{s}_p\hat{n}_q + \hat{s}_q\hat{n}_p)d^e(t'-t_0') \end{aligned} \tag{22}$$

Here, $d(t'-t'_0)$ is a unit function that describes the shape of the source slip function, and the superscript indices u and e refer to the large and egf earthquakes. $d(t'-t'_0)$ is sometimes represented as a ramp-like function, set equal to zero before the onset of slip at time t'_0, and for which the time interval when slip occurs is called the rise time. For an impulsive point source, the rise time is instantaneous, and $d(t'-t'_0)$ takes the shape of a Heaviside unit-step function. It is common to apply the deconvolution method in the frequency domain, where the deconvolution transforms to division, thus simplifying the calculations. Equation (22) can then be written in the frequency domain as

$$\frac{u_n(X,\omega)}{e_n(X,\omega)} = \frac{M_0^u(\hat{s}_p\hat{n}_q + \hat{s}_q\hat{n}_p)D^u(\omega)}{M_0^e(\hat{s}_p\hat{n}_q + \hat{s}_q\hat{n}_p)D^e(\omega)}, \tag{23}$$

where D(ω) is the Fourier transform of $d(t'-t'_0)$. If we further assume that both events have the same focal mechanism solution, we have

$$\frac{u_n(X,\omega)}{e_n(X,\omega)} = \frac{M_0^u}{M_0^e}\frac{D^u(\omega)}{D^e(\omega)}. \tag{24a}$$

It should be pointed out that this representation holds even when there is a component of slip perpendicular to the fault surface (Equation 3a)—that is, even if the faulting mechanism is not purely a shear mechanism—as long as both the large earthquake and the EGF earthquake have the same focal mechanism, so that it will cancel out when the deconvolution or the spectral division is performed.

The displacement field solved for a general second-order symmetric moment tensor (point source) solution in an infinite homogeneous medium shows three relative-magnitude terms that depend on the source-receiver distance: near-field, intermediate-field, and far-field (Aki and Richards, 2002, eq. 4.29). In the far-field term, the shape of the displacement pulse is proportional to the particle velocity at the source averaged over the fault plane. The displacement field can then be approximated by its far-field representation, and the particle slip-time function at the source $d(t'-t'_0)$ can be approximated by the particle velocity-time function at the source $\dot{d}(t' - t'_0)$. If the source slip function has a ramp or Heaviside function shape, the displacement pulse, or far-field source-time function, will have a boxcar or a delta Dirac function shape, respectively. Equation (24a) can then by expressed as

$$\frac{u_n(X,\omega)}{e_n(X,\omega)} \approx \frac{M_0^u}{M_0^e}\frac{\dot{D}^u(\omega)}{\dot{D}^e(\omega)} = \frac{M_0^u}{M_0^e}\dot{D}'(\omega). \tag{24b}$$

$\dot{D}'(\omega)$ is the far-field unit-normalized relative source-time function; its amplitude is proportional to the ratio of the moments. If we inverse-transform to the time domain, we get $\dot{d}'(t')$, the far-field relative source-time function. Often, small earthquakes have moments greater than the threshold necessary to be effective impulsive point sources. However, if both earthquakes share the same focal mechanism, the deconvolution method can still be applied. Care must be taken, however, when measuring source durations from the source pulses, because it is a relative duration. Figure 2 shows a deconvolution of a M = 3.5 earthquake with a M = 2.3 earthquake, and the inverse transform to the time domain to

obtain $\dot{d}'(t')$. If the smaller event is not effectively an impulsive point source, then we can only achieve relative values for the larger event.

Kinematic Earthquake Models and Synthesized Ground Motion Using Empirical Green's Functions

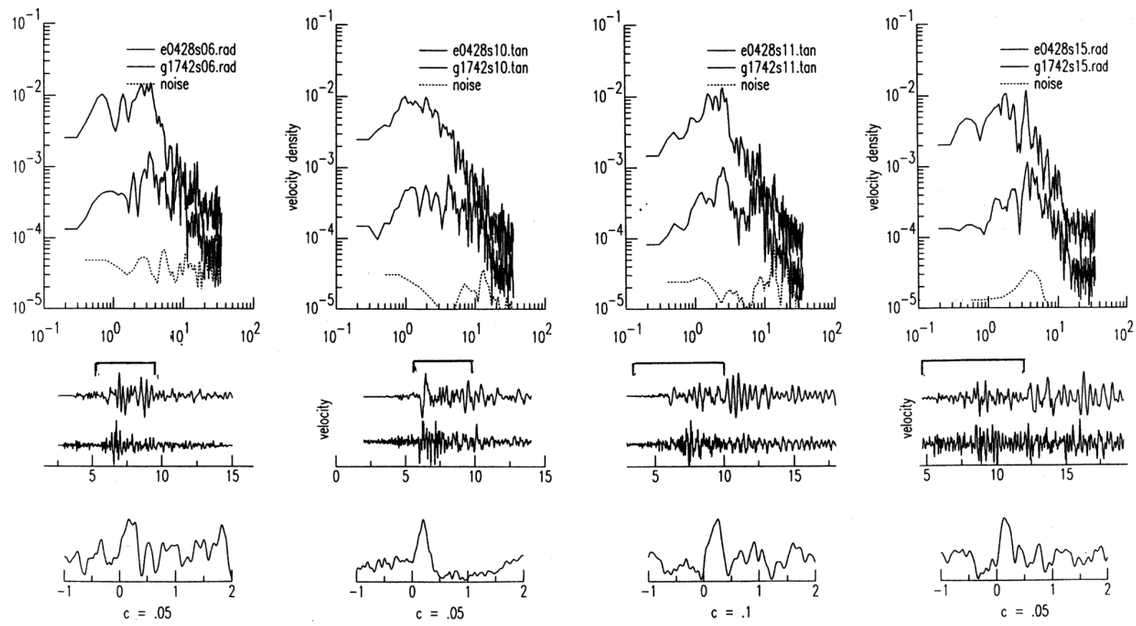

Fig. 2. Deconvolution at four stations of a M3.5 larger earthquake with a M2.3 earthquake, which is assumed to be effectively an EGF. *Top:* velocity spectra of both earthquakes. *Middle*: recorded velocity seismograms and time window used in the analysis. *Bottom*: relative source time function rate (from Hutchings, 1991).

3. Observations of Empirical Green's Functions (EGFs)

By the definition stated previously in section 2.0, Equation (9), EGFs are recordings of earthquakes for which the effects of rupture and size cannot be observed in the frequency range of usage. This definition provides a basis for understanding the influence of frequency band, geology, and the source rupture on recorded seismograms used as EGFs. Theoretically, the Fourier amplitude spectra of displacement will be flat up to a source corner frequency, which is inversely proportional to the duration of the earthquake rupture. The duration of an earthquake is dependent on the fault dimensions and the earthquake rupture process. A flat Fourier amplitude spectrum is the result of a zero duration source, or source with shorter duration than the period of the highest frequency in the spectrum. Therefore, seismograms filtered to include frequencies below their source corner frequency exclusively do not include the effects of duration, and they will effectively be impulsive point sources for that frequency range. If they are also located close to one another and have the same focal mechanism solution, they will have nearly identical waveforms over that frequency range. In fact, waveform similarity is the best selection criteria for a good EGF earthquake.

Figure 3 shows several recordings of earthquakes along the Hayward fault in California with very closely located hypocenters and nearly identical focal mechanisms, but varying moments. The earthquakes range in magnitude from 1.8 to 4.1 and the recorder is 10 km

distant. The dimension of the sources ranges from about 20 m to 500 m. Also shown are the Fourier amplitude spectra of the recordings (Figure 3c). It is apparent that the source corner frequency decreases for larger magnitude earthquakes, and that all spectra are approximately flat below 2 Hz. Unfiltered (Figure 3a), the records appear quite different. However, when filtered to include only frequencies less than the corner frequency (Figure 3b) of the largest earthquake (2 Hz), they appear nearly identical, and are effectively from point sources.

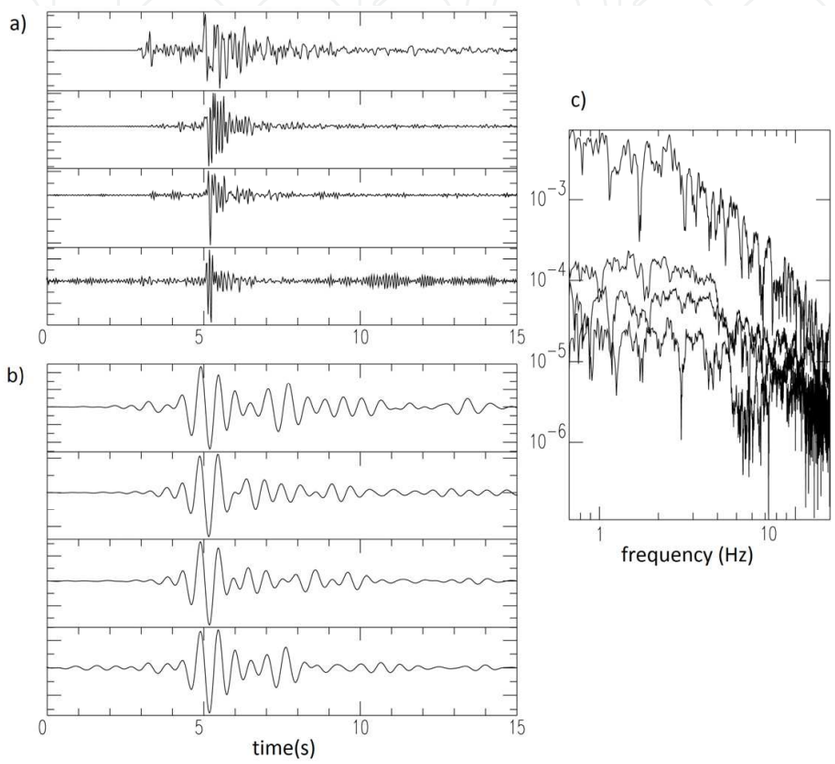

Fig. 3. (a) Unfiltered records of events with different magnitudes that occurred at approximately the same location along the Hayward fault and were recorded at the same station (YBI). (b) Band-pass filtered between 1.0 Hz and 2.0 Hz, for which there is no source effect and signal to noise is good. (c) Fourier amplitude spectra of the recordings.

The use of EGFs has to be quantified for the low frequency end of the spectrum as well. Most recordings of small earthquakes are band limited by cultural noise or instrument response, and do not include frequencies below about 0.5 Hz, so that full broadband use of EGFs is not generally possible. This is the frequency range wherein near-field terms are important for source studies and strong ground-motion synthesis. However, it has long been recognized that synthetic seismograms can be accurately calculated for frequencies less than 0.5 Hz in areas where the geology is well known. Often, tomographic inversion for velocity structure provides the basic information necessary to accurately synthesize low-frequency seismograms (Gök and Hutchings, 2004). Thus, there is a convenient match between the synthetic Green's functions that can be accurately calculated for frequencies commensurate with the scale in which the geology can be well known, and can include the near-field wave propagation effects that are difficult to record—and the EGFs that record

the high frequencies for which the geology is not well known and for which primarily far-field arrivals are important. Merging the two frequency bands provides a broadband simulation, so that synthetic Green's functions can be used for frequencies 0.0 to about 0.5 Hz, and EGFs can generally be used for frequencies from about 0.5 to 25.0 Hz (or higher for stable continental interiors). This covers the frequency range of engineering interest.

3.1 Scaling relations

A significant subject in seismology is how earthquakes scale—that is, whether earthquakes are self-similar and follow a constant scaling relationship (constant stress drop) between the earthquake moment and its size, or whether there is a non-constant scaling relationship. Constant stress drop is widely accepted as a first-order approximation for large and moderate earthquakes (Aki, 1967), although stress-drop values show a wide variation from about 0.1 MPa to 100 MPa (e.g., Hanks, 1977). However, a non-constant scaling relationship has been proposed for small earthquakes, based on the observation of a small systematic shift to lower apparent stress (scaled energy multiplied by the medium rigidity) at lower magnitudes (Figure 4). Energy scaling relationships remain unresolved. There are contradictory studies arguing for self-similarity where scaled energy and apparent stress are constant (e.g., McGarr, 1999; Ide and Beroza, 2001; Ide et al., 2003) and for non-self-similarity where scaled energy decreases with earthquake size (e.g., Abercrombie, 1995; Prejean and Ellsworth, 2001; Mayeda and Walter, 1996). This decrease in scaled energy suggests differences (with earthquake size) in frictional behavior during rupture (Kanamori and Heaton, 2000).

The scatter in stress-drop estimates reflects the different tectonic regimes in which the earthquake occur, variations within a regime, the diversity of methods used to retrieve source parameters, data quality, and the available bandwidth. Uncertainties in stress-drop estimates propagate from seismic moment and source-dimension estimates, since stress drop is directly proportional to seismic moment and inversely proportional to the source dimension cubed (see Equation 33). Today, most methods estimate seismic moment within a factor of 2, but there are still huge uncertainties in fault-dimension estimates. Fault dimension is determined from the corner frequency in spectral analyses or, alternatively, from the source duration in time analyses (see equations 31 and 32, respectively). Retrieving accurate small-earthquake corner frequencies is particularly challenging, because it requires path and site effects corrections, which are not easily determined. Also, good-quality data with high-frequency content is required to estimate corner frequencies of small to moderate earthquakes. Limited bandwidth introduces a false cut-off at high frequencies and a bias in earthquake selection, leading to the underestimation of corner frequency. In addition, attenuation-corrected corner frequencies are higher than the observed corner frequencies (Hough et al., 1989; Anderson, 1986; Ide et al., 2003). Consequently, uncorrected corner frequencies lead to an underestimation of stress drop and could be responsible for an apparent non-constant scaling relationship. Historically, the bias in stress drop and thus the non-constant scaling relationship introduced by an inaccurate corner frequency (or rupture duration) estimate was argued by many to be a source effect and not a path effect. To date, the EGF deconvolution method is the best available method for retrieving accurate earthquake source properties, because it empirically corrects for path and site effects. Nevertheless, it depends on the quality of the EGF, which many studies to not adequately test.

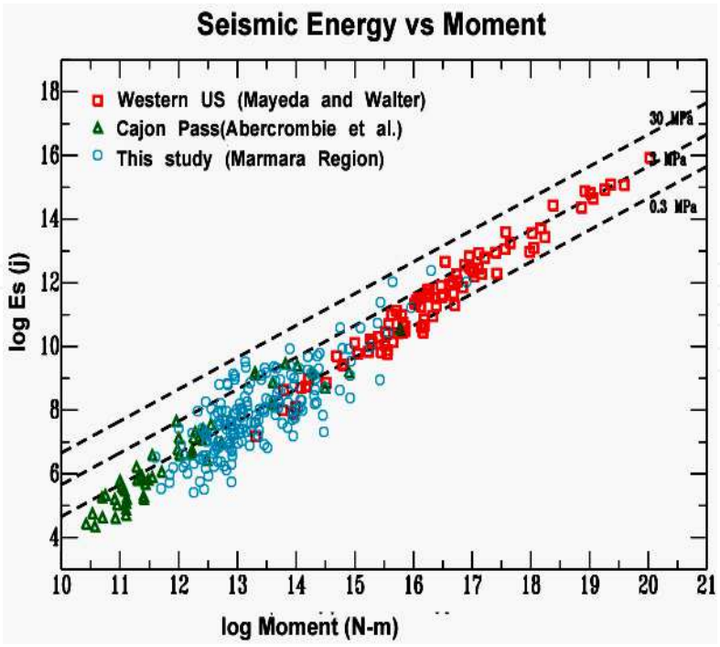

Fig. 4. Moment and energy estimation from several studies, and line of constant stress drop. A decrease in stress drop with decreasing earthquake size is observed within each dataset. (Abercrombie, 1995; Mayeda and Walter, 1996; Gök et al., 2003) These studies used a similar approach to calculate energy, so that if there is a bias in the approach, then the possibility exists that small earthquakes are plotted at lower energy values than they should be, thus causing the apparent shift. (figure from Gök et al., 2003).

3.2 *fmax*, κ, and *t**

Parameters *fmax*, κ (kappa), and *t** (t-star) are important parameters used in understanding EGFs. The corner frequency of spectra is usually observed on log-log plots, and *fmax* is an observed corner frequency of spectra that is constant for different sizes of earthquakes. A Brune source model with 10 MPa stress drop predicts a source corner frequency of 10 Hz and 25 Hz for events with moment of 1.0×10^{14} Nm and 1.0×10^{13} Nm, respectively. However, such events generally are observed to have the same corner frequency near 10 Hz. Recently it has been shown that this constant corner frequency is due to attenuation, where the source corner frequency is much higher than can be observed in the frequency range recorded, so only the effect of attenuation is observed. If the spectra is plotted on a log-linear scale, the plot is a straight line and the slope is called κ. So, below a certain size earthquake, when the source corner frequency is very high, *fmax* and κ are measures of the filtering effect of the site geology.

Parameters κ and *fmax* are not a physical model for attenuation. A common interpretation is that attenuation is caused by absorption of energy expressed by the well-known seismic quality factor Q, such that $e^{-\omega(R/Qv)}$ is the attenuation operator in the frequency domain, where R is travel distance, v the seismic velocity, and ω the angular frequency. The terms in parentheses have units of time and are often referred to as *t**. Therefore,

$$e^{-\omega(R/Qv)} = e^{-\omega\kappa} = e^{-\omega t^*} . \tag{25}$$

However, t^* generally refers to any path attenuation operator between the earthquake and the site, and κ generally refers to the attenuation just beneath a site, and is often equated with a site characterization (Anderson and Hough, 1984) ; *fmax* is the resulting effect of attenuation and is generally assumed to be caused by the same near-site attenuation as κ. However, in reality, *fmax* can result from any whole-path attenuation effect that acts as a filter and limits the frequency band of observations. Baise et al. (2001) observed, for example, that the whole-path attenuation band limited recordings in a 61 m borehole at Yerba Buena Island in San Francisco Bay to about 3 Hz, such that events as large as magnitude 4.0 have essentially the same observed corner frequency as the smallest events that could be detected (M2.0). They attributed this to a regional effect of a heterogeneous and highly attenuating Franciscan formation.

Hanks (1982) and Anderson and Hough (1984) found the threshold moment for constant κ and f*max* to be about 1.5×10^{14} Nm. Interestingly, Hutchings and Wu (1990) plotted pulse widths of the first arriving P-waves and found the same effect, a constant pulse width below a moment threshold of 1.5×10^{14}. Once a source pulse of an earthquake is generated, it broadens as it propagates due to attenuation. This threshold is dependent on the geology, and for boreholes the threshold can be substantially lower.

Abercrombie (1998) addresses the apparent paradox that *fmax* is near 10 Hz, no matter what the geology of the site region. Her borehole and literature analysis concludes that micro-cracks in the geology that occur due to the diminishing lithostatic load near the surface causes intrinsic attenuation, which is essentially the same regardless of the geology. This results in a Q of about 10 to 100 near the surface. Inelastic attenuation, attributed to energy absorption, is very low at greater depths, and intrinsic attenuation is minimal as well, so the combined Q approaches 1000. Very near the surface, inelastic attenuation in soft soils causes significant loss of energy.

Some authors have attributed this constant maximum corner frequency to be the result of a minimum source dimension for earthquakes, which would result in a decrease in stress drop for smaller events (Archuleta et al., 1982; Archuleta 1986; Papageorgiou and Aki, 1983). However, a wide body of literature supports the interpretation that the constant maximum corner frequency (or minimum source dimension) results from whole-path or near-site attenuation. First, several authors have noticed that this apparent maximum corner frequency was different at different recording sites, so that it had a site dependence and not a source dependence (Anderson and Hough, 1984; Frankel and Wennerberg, 1989; Hutchings and Wu, 1990; Blakeslee and Malin, 1991; Aster and Shearer, 1991). Further, Abercrombie (1995) estimated source corner frequencies from events recorded in granite at a depth of 2.5 km in a Cajon Pass scientific drill hole, avoiding the highly attenuating surface layers, and observed corner frequencies about a factor of 10 higher than observed at the surface. They attributed this to near-surface attenuation. Abercrombie also observed that corner frequencies of recordings at depth continued to increase with decreasing seismic moment and found to that they follow self-similarity. Prejean and Ellsworth (2001) made the same observations about near-surface attenuation and increasing corner frequencies with decreasing moments, from a 2 km deep borehole in the Long Valley Caldera. These observations are supported by previous, less definitive studies (Malin and Walter, 1985; Hauksson et al., 1987; Aster and Shearer, 1991). In sum, the overriding evidence is that attenuation near the surface of the crust acts as a filter on recordings of seismograms, limiting the observable maximum corner frequency—so that this apparent non-constant stress-drop scaling was caused by path effects. However, the non-constant scaling of scaled energy referred to in the previous section is apparent after the (more

or less successful) removal of all path and bandwidth effects, so that the controversy regarding source scaling still continues. Until uncertainties in energy measurements can be significantly reduced, the issue will not be resolved.

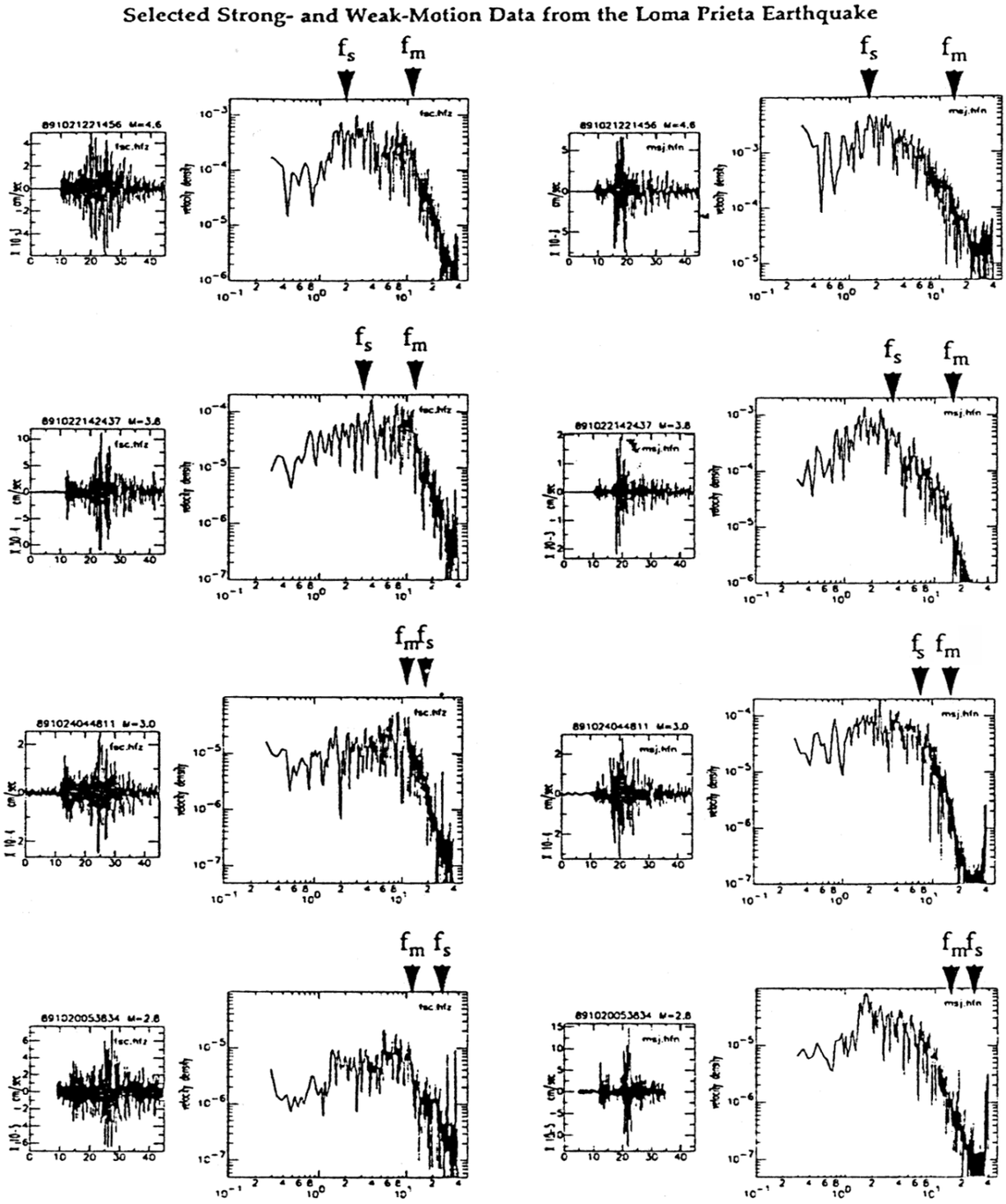

Fig. 5. Events of different magnitudes recorded at two different locations. *fmax* (f_m) is different for each site, but remains the same as events change in magnitude. The source corner frequency (f_s) gets smaller as the magnitudes increase.

The parameter *fmax* provides a convenient threshold for EGFs. Recordings of events below the threshold moment do not have significant effects due to the source; i.e., the true source corner frequency is higher than *fmax*. Hutchings and Wu (1990) confirmed this by showing that events located very close to each other, with the same focal mechanism solution and with moments below the threshold for *fmax*, had virtually identical waveforms that scaled linearly in amplitude only with differences in their moments. Figure 5 shows several events at the same location with moments above and below the threshold. The source corner frequency and *fmax* corner frequencies are plotted in the figure. As the events get smaller and smaller, the source corner frequency moves to higher frequencies, but the *fmax* corner remains the same. An interesting question regarding *fmax* is that if there is a spectral fall-off caused by attenuation and an apparent source corner frequency in the spectra, then there should be an additional fall-off at frequencies above the actual source corner frequency (Jarpe et al., 1989). This is apparent in Figure 5.

3.3 Finite bandwidth

The fact that earthquake records are limited by finite bandwidth can introduce significant bias when solving for scaling relationships. The sampling rate constrains the dataset resolution (Nyquist frequency) of the maximum corner frequency and smallest pulse duration that can be observed. The recording instrument characteristics also constrain the lowest frequency for which signals can be recorded. Therefore, when choosing the small events in a data set, we are limited to observing corner frequencies less than the maximum frequency exclusively, and we are thus biased because higher corner frequency events are excluded. The opposite will happen for the selection of the largest magnitude earthquakes in the dataset. In that case, the selection bias is choosing only lower corner frequencies. Also, in subsequent interpretation, very high and very low stress drop events will be excluded. Figure 6 shows the effect of the high frequency bias. The red dots that plot in a straight line show the upper limit of stress drop that can be interpreted with a Nyquist frequency of 80 Hz. The "true" corner frequency of these events is above the line. The other red dots are the result of an EGF study. They show a scatter with a slope trending parallel to the upper limit straight line. Viegas et al. (2010) pointed out that the apparent slope of the stress values as a function of moment is due to the elimination of higher stress drop values imposed by the Nyquist frequency.

The blue dots in Figure 6 show stress drop values obtained with non-EGF approaches. In this case, researchers have to model attenuation which is very often done incorrectly and subsequently cause an apparent corner frequency. There is a large trade-off between attenuation and apparent corner frequency (Anderson and Hough, 1984), and many possible combinations of these two variables provide equally good fits to the source spectra data (Hough et al., 1991). The EGF method uses the actual attenuation, so it does not suffer from this effect. The incorrect estimation of attenuation can result in miss identification of the source corner frequency. Such is apparent the case of the blue dots as they show a parallel line to upper limit imposed by the Nyquist frequency. In this case the calculated attenuation value systematically forced an apparent corner frequency just below the Nyquist frequency. So, the apparent stress drop variation as a function of moment is due to the upper limit of imposed by the Nyquist frequency and the choice of attenuation and not a source effect. This may be one of the causes of interpretations of stress-drop scaling with magnitude (see section 3.1). Ide and Beroza (2001) showed that most of the dependence on

size interpreted for small earthquakes in apparent stress versus seismic moment relationships results from limited bandwidth.

The finite nature of the bandwidth has also to be taken into account when applying the EGF method in the time domain. The duration of the delta function has to be estimated based on the sampling rate and number of points needed to represent it, so that only earthquakes with source durations above the delta function are considered, and a bias toward decreasing stress drop with decreasing moment is avoided.

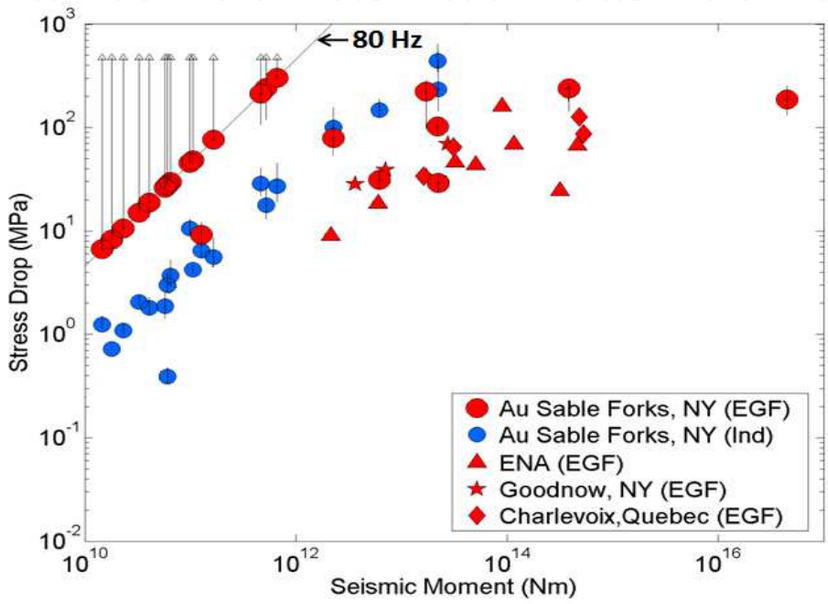

Fig. 6. Stress drop versus Seismic moment. Comparison of stress drop results obtained with the EGF method (red symbols) with the ones obtained with an individual fitting method (blue circles). All results were converted to a Madariaga (1976) source model for comparison purposes. Arrows indicate a minimum stress drop estimate. Data points are: Au Sable Forks, NY (EGF and Ind, Viegas et al., 2010); ENA (Shi et al., 1998); Goodnow, NY (Xie et al., 1991); Charlevoix, Quebec (Li et al., 1995). (Adapted from Viegas et al., 2010).

4. Earthquake source parameters

Earthquakes are characterized by their source parameters, such as hypocentral location, equivalent fault radius, stress drop, apparent stress, radiated energy, and focal mechanism. These parameters are routinely determined for most moderate to large events (>M4) in a straightforward way. Events are usually well recorded by regional seismographs and often with broadband recording capabilities, with frequencies as low as 0.1 Hz or even 0.01 Hz. Moments are easily calculated from the long period asymptote on displacement spectra (Aki and Richards, 2002, sec. 3.4) or by moment-tensor inversion programs (Dreger, 2003; Pasyanos et al., 1996). Corner frequencies, from which source dimensions are calculated, are mostly less than 0.5 Hz (depending on the tectonic setting), below frequencies for which there are significant site response and attenuation effects on their spectra. For these events, corner frequencies can be identified by the intercept of the flat, low-frequency portion of displacement spectra with the near ω^{-2} fall-off of the higher frequencies. A second corner frequency (*fmax*, discussed above) is separated enough in the spectra from the source corner

frequency that misidentification or interference is unlikely. Calculating hypocentral location and focal mechanism solutions are not discussed here. Typically, earthquakes are recorded by local or regional networks and these parameters can be well constrained. Estimating these parameters is well described in many textbooks (e.g., Lay and Wallace, 1995).
Determining the moment and source corner frequency of smaller earthquakes is much more difficult. Source corner frequencies of small events are higher than 1 Hz and must be determined from the portion of the spectra that are greatly affected by site response. The spectra of small events are usually band-limited by cultural noise, so only frequencies above ~0.2 to 0.5 Hz and below about 15 to 25 Hz are usually recorded for surface sites. This is the frequency band for site response and near-surface attenuation effects on spectra can be significant. Even frequencies as low as 0.2 Hz for soil sites are effected by site response (Jarpe and Kasameyer, 1996; and Bonilla et al., 1997). Further some rock sites can also have a significant site response effect (Steidl et al., 1996). It is in determining the source parameters of small earthquakes that EGF methods prove to be particularly useful, because propagation-path and site-response effects are empirically removed.

4.1 EGF methods for determining source parameters

Here we discuss the EGF method for determining source parameters, whereby a small earthquake located in close proximity to a larger earthquake, and with the same focal mechanism, is used to remove the propagation path and site response from the records of the larger earthquake. Although all EGF methods share the same basic principles, there are variations in the way the method is applied. It can be applied in the frequency domain, time domain, or both, using direct, surface, or coda waves, to a single pair of earthquakes at a time or to multiple earthquakes simultaneously. In this section, we briefly review the various EGF methods, indicating their main advantages and disadvantages.

4.1.1 Frequency domain EGF

The EGF method was initially applied in the frequency domain and was designated by a spectral ratio method. Bakum and Bufe (1975) were one of the first to use the method to determine attenuation characteristics for propagation paths along the San Andreas Fault trace. The method was further developed and applied to source studies (e.g., Frankel 1982; Mueller, 1985; Hutchings and Wu, 1990; Hough et al., 1991; Abercrombie and Rice 2005; Viegas et al., 2010) commonly used today.
The source spectral ratio of P or S wave radiation between two earthquakes is calculated assuming a point-source approximation. First, the complex Fourier spectra of the displacement records are calculated, after correcting for instrument response. The theoretical far-field P and S wave radiation from a point source is calculated by solving Equation (7) for the specific wave type motion (P, SH, SV). The Fourier amplitude displacement spectra of P or S wave displacement records can be modeled using the theoretical spectrum equation (Brune, 1970)

$$\Omega(f) = \frac{\Omega_0 \, \mathrm{e}^{-\frac{\pi f t}{Q}}}{\left[1 + \left(\frac{f}{f_c}\right)^{\gamma n}\right]^{\frac{1}{\gamma}}}, \tag{26}$$

where $\Omega(f)$ is the displacement amplitude spectrum, Ω_0 is the long-period level (or asymptote) of the spectrum, f_c is the corner frequency, t is the travel time of the seismic wave of interest (P or S), Q is the frequency-independent whole-path attenuation quality factor, and γ and n are constants that control the shape of the spectrum curvature around the corner frequency and the high frequency fall-off, respectively. For γ =1 and n = 2, Equation (26) corresponds to the Brune (1970) source model, and γ = n = 2 corresponds to the modified Boatwright (1980) source model. Boatwright's spectrum has a sharper corner frequency than Brune's. There is no rationale for which spectral model to chose; usually, the spectral shape that best fits the observed spectrum is the one used. Although an approximation to a one-corner theoretical spectra is usually assumed, theoretical source spectra should have two corner frequencies, one representing the particle dislocation history or rise time, the other representing the fault finiteness. Depending on the fault geometry and slip history, the two corners will be closer in frequency or further apart, thus being better approximated by a sharper or smoother one-corner frequency model, respectively. $e^{(-\pi ft/Q)}$ is the attenuation operator and is equal to 1 for null attenuation ($Q \to \infty$). After calculating the complex spectra of both earthquakes, the complex spectral division is performed. The corresponding amplitude spectral ratio, $\Omega_r(f)$, can be modeled using (Abercrombie and Rice, 2005)

$$\Omega_r(f) = \Omega_{0r}\left[\frac{1+\left(\frac{f}{fc_2}\right)^{mn}}{1+\left(\frac{f}{fc_1}\right)^{mn}}\right]^{\frac{1}{\gamma}}. \tag{27}$$

Equation (27) represents the theoretical spectral ratio and corresponds to the division of the large earthquake by the EGF earthquake theoretical source spectra, as described by Equation (23), assuming that the attenuation operator is the same for both spectra. fc_1 and fc_2 are the corner frequencies of the large and EGF earthquakes, respectively, and Ω_{0r} is the relative long-period level (or asymptote). The spectral ratios are modeled in a bandwidth within which there are good signal-to-noise ratios for both earthquakes, which usually corresponds to the usable bandwidth of the EGF earthquake, since the larger earthquake has a stronger signal over a wider frequency band. The spectral ratio is modeled so that the corner frequencies of both earthquakes and the ratio between the two long-period levels are obtained. The spectral ratio is usually fit with Equation (27) using some type of nonlinear regression, so that the objective function that measures the differences between the model and the data is minimized. Viegas et al. (2010) minimized the function

$$res = \sum_{i=1}^{N}\left(\log\Omega_{rM}(f_i) - \log\Omega_{rD}(f_i)\right)^2, \tag{28}$$

where the indices M and D refer to model and data, respectively, and N is the number of points in the spectral ratio, using a Nelder-Mead simplex method.

Some studies additionally perform an inverse Fourier transform of the complex spectral ratio back to the time domain, to obtain the earthquake's far-field relative source-time function (e.g., Tomic et al., 2009; Viegas et al., 2010; Viegas 2011). A clear source pulse would indicate that the EGF is sufficient in both amplitude and phase. If the corner frequencies of the two earthquakes are different by a sufficient value, and the signal-to-noise ratio is adequate over a broad-enough frequency range, this method offers the opportunity to simultaneously extract the

corner frequencies of both earthquakes, after having the path effects removed. However, Abercrombie et al. (2012) found that the corner frequency of the smaller earthquake in the ratio (EGF) is often underestimated. A good approach is to use successive smaller earthquakes as EGFs of succesivelly smaller earthquakes until the resolution limit is reached. Figure 7 exemplifies the EGF spectral-ratio-fit analysis applied to two pairs of aftershocks of the M5 2002 Au Sable Forks, NY, earthquake. Two examples are shown, one in which the corner frequency of the EGF earthquake is outside the bandwidth and cannot be determined, and another in which the corner frequencies of both earthquakes are within the usable bandwidth and can be determined.

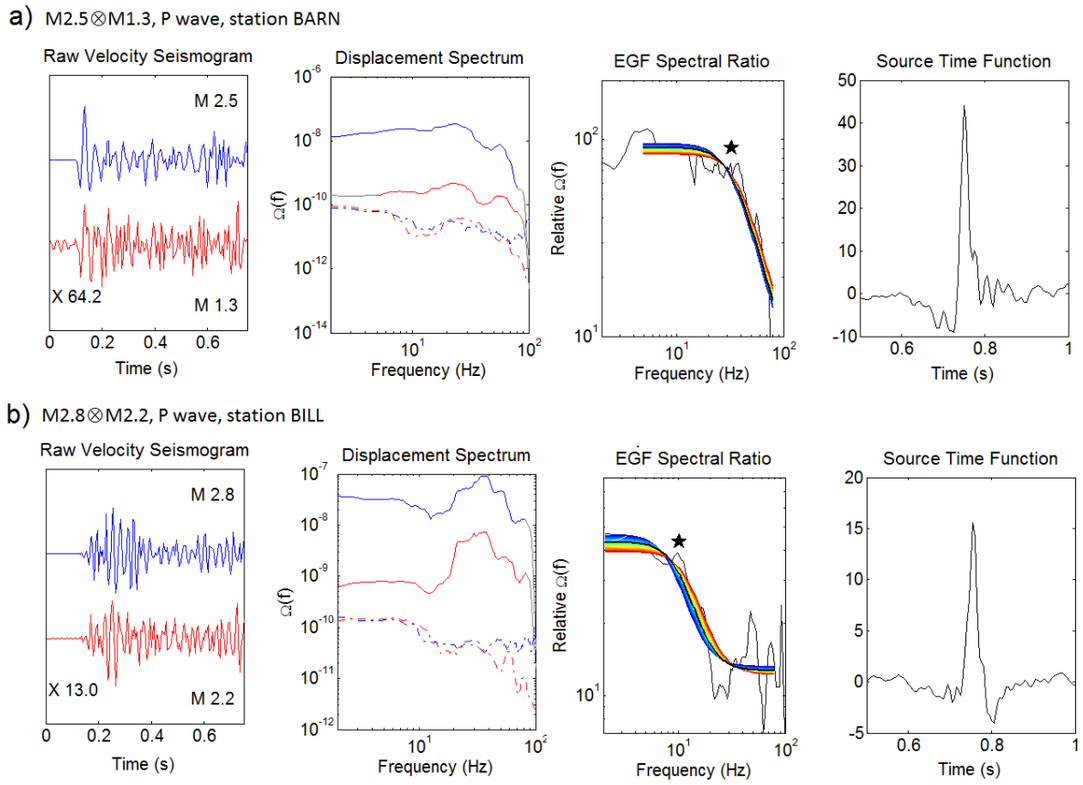

Fig. 7. EGF spectral-ratio-fit analysis. Example of the EGF spectral-ratio-fit analysis of two small earthquakes (P waves). *Left panel:* P wave raw velocity seismograms of the two aftershocks of the M5 2002 Au Sable Forks, New York, USA, earthquake. The number on the bottom left corner of the plot indicates the multiplication factor applied to the EGF record to match the amplitude of the larger earthquake Magnitudes are indicated on the right. *Central left panel:* Calculated displacement spectra of the seismograms on the left panel, after integration and instrument correction. The full lines correspond to wave signal and the dotted lines to pre-P noise. *Central right panel:* Best fit (thick black line) model to the spectral ratio (thin black line). The star indicates the best-fit corner frequency of the larger earthquake. *Right panel:* Obtained Earthquake source time function (adapted from Viegas et al., 2010).

4.1.2 Time domain EGF

The EGF time-domain deconvolution method is also commonly used in the time domain (e.g., Frankel and Kanamori, 1983; Frankel *et al.*, 1986; Mori and Frankel, 1990; Mori et al.,

2003). Figure 2 shows source pulses obtained through the time deconvolution of two similar seismograms. Once the pulse duration is measured, the source dimension can be estimated. Care must be taken in measuring the source pulse, since it is a relative source pulse. Even if the EGF is an effective impulsive point source, because discrete time series are being used and are subjected to a certain sampling rate (and Nyquist frequency) and filtering techniques, the delta function will have a minimum duration greater than three data points. This effect will decrease the relative duration of the source pulse. A large difference in magnitude between the two earthquakes, such that the duration of the target earthquake is many times that of the EGF earthquake (or delta function), will help minimize these effects. Some attention must also be paid to measuring the onset of the pulse, because noise introduces ambiguity in the deconvolved trace. Some studies use the zero crossing as the onset, others the change in gradient. Mori et al. (2003) picked the onset of the pulse on the original data, which is usually clearer, and then calculated the pulse start time.

4.1.3 Multiple EGFs

When dealing with large datasets, investigators find it preferable to apply the EGF method simultaneously to a large number of earthquakes. Hough (1997) first proposed the method called Multiple EGF (see Section 4.3 below), which was adopted by later studies with slight changes (e.g., Hough et al., 1999; Prejean and Ellsworth 2001; Ide et al., 2003). The method is the same as the standard spectral-ratio EGF method for determining source parameters, but takes advantage of multiple records in the inversion for attenuation. Here, it simultaneously inverts for kappa using a cluster of closely located earthquakes constrained by the calculated EGF source parameters. Using large numbers of same-station records for clustered earthquakes decreases the uncertainty in the source-station attenuation estimates.

Prieto et al. (2004) used a stacking approach to estimate source parameters of over 400 M0.5–to-M3.4 earthquakes recorded in southern California, following the method developed by Warren and Shearer (2002) to calculate upper mantle attenuation. The method takes advantage of a large dataset in which there are multiple receivers for each source and multiple sources for each receiver. Prieto et al. uses several events recorded at one station to calculate the site response. They do this for all stations. Then, source parameter for a single earthquake recoded at many stations is determined by simultaneously fitting all corrected spectra (Andrews, 1986; Boatwright et al., 1991). The process is repeated iteratively until a best solution is found. The obtained source spectra of all the events are relative stacked spectra and need to be scaled to absolute values using magnitude information. So, the spectra are averaged in magnitude bin intervals and corrected for attenuation by using the smallest bin spectrum as an EGF for the larger moment bin spectra.

The stack method has been applied to a few large datasets. Shearer et al. (2006) used it to determine the source parameters of 68,803 events of M_L0.5 to M_L 5.2 recorded in Southern California between 1989 and 2001. In that study, the authors used a theoretical spectral shape to fit the stacked spectra and solve for the EGF, instead of using the smallest bin spectrum as an EGF, so that lower-magnitude bin spectra close to the minimum bin magnitude could be used. Allmann and Shearer (2007) applied this method to determine temporal and spatial stress-drop variations in 42,367 earthquakes recorded between 1984 and 2005 within the Parkfield segment of the San Andreas fault, and Allmann and Shearer (2009) applied it to determine global variations in stress drop using ~2,000 >M5.5 earthquakes recorded globally between 1990 and 2007. Because it deals with such huge datasets through staking, grouping, and averaging, this method can only resolve average

source properties, limited by theoretical source models and average velocity models. However, the relative variations in stress drop between earthquakes are robust, and the method is efficient when looking for spatial and temporal changes within large datasets.

4.1.4 Coda EGF

Mayeda et al. (2003), Baltay et al. (2010), and Viegas et al. (2011), among others, have used a version of the EGF deconvolution method to obtain earthquake source parameters using coda waves. Coda waves are waves that were backscattered multiple times from numerous heterogeneities in the earth and arrive later in the seismogram. Because coda waves sample the crustal volume multiple times they can provide an average model of the geology and the earthquake source, since all source directivity and radiation effects were averaged out. The Fourier amplitude source spectra derived from coda waves is dimensionless and independent for each frequency band and needs to be tied to some form of a theoretical model to get the shape of a source spectra and seismic moment units. First, "calibration events" are selected for which independent moment estimates are available. These usually are the larger events in the dataset. Then, a source spectral shape is estimated for the calibration events by choosing a stress drop, and thus a corner frequency. The Fourier amplitude spectral values estimated from the coda that don't fall on the theoretical plot are assumed to be representative of the site response. This term is subtracted from all the other spectra. If the original estimation of stress drop is correct, then the spectral shape from the smallest event will be flat up to its high corner frequency. If it is not flat, then a different stress drop is estimated, and the process is repeated until all the events are flat below their corner frequencies (Walter and Mayeda, 1996). This can be seen as an EGF approach, where the spectral shape of the smallest earthquake, which is mostly flat, is used to correct the spectra of the larger events. For an effective point source, the EGF spectra must be

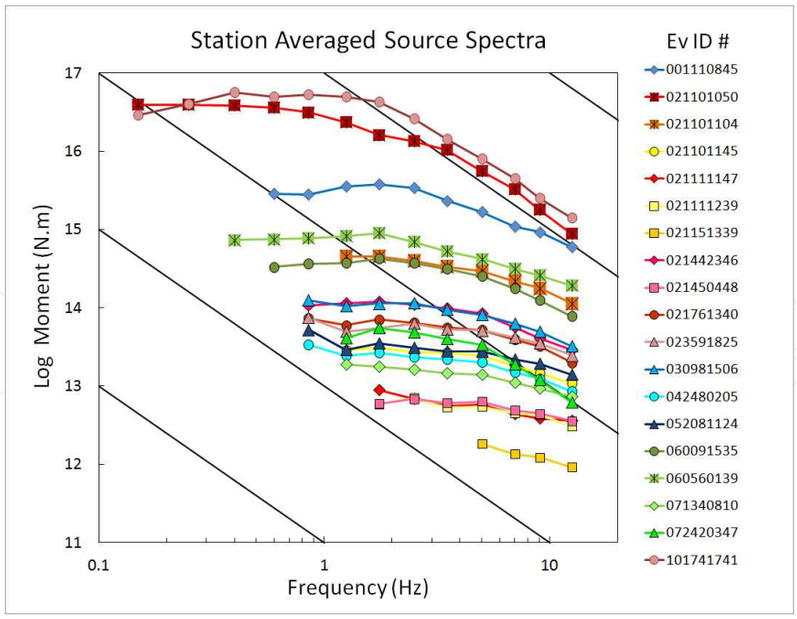

Fig. 8. Coda-derived earthquake source spectra for a series of M2 to M5 Eastern North America earthquakes. The earthquakes used as magnitude calibration events are plotted with a square plus a cross symbol. An apparent stress drop of 10 MPa was used for the theoretical spectra (from Viegas et al., 2011).

completely flat within the available bandwidth, but this is not the typical case, and corner frequencies are usually modeled by assuming a certain stress drop (Figure 8). Although minimal, this assumption can propagate to the other spectra and bias the corner frequency estimates. To avoid this, Mayeda et al. (2007) and Viegas (2009) started using spectral ratios from coda-derived individual source spectra. Figure 9 shows coda-derived spectral ratios for Parkfield, California, USA, earthquakes using the same M1 EGF with two M2 earthquakes. The advantage of using coda waves is that because of its averaging properties, source parameters can be estimated from a single station, the equivalent to a 9- to 25-station network average using direct waves (Mayeda et al., 2003). The big disadvantage of using coda waves is that precisely because of its averaging properties, source directivity cannot be determined, and the fault plane cannot be identified.

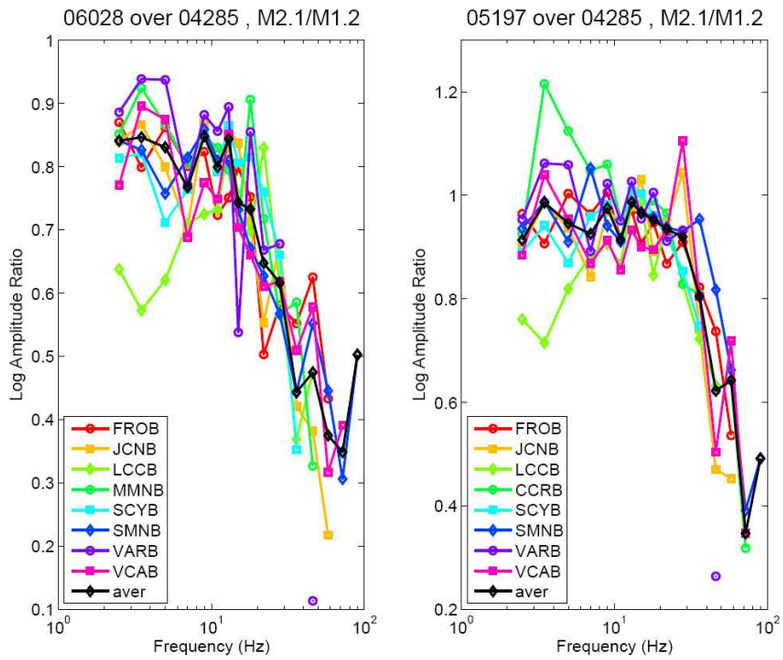

Fig. 9. Amplitude spectral ratio for two Parkfield target earthquake pairs (M2.1/M1.2) at several stations. The black line with diamonds is the average spectral ratio (from Viegas, 2009).

4.1.5 EGF earthquake selection criteria

The selection of a suitable EGF earthquake is fundamental to obtaining reliable source parameters. The basic criteria of using as an EGF (1) a collocated earthquake with (2) a similar focal mechanism that (3) is at least one order of magnitude lower than the target earthquake assure well-constrained source parameters. The fulfillment of criteria requirements (1) and (2) can be verified through waveform similarity, confirming that the waveforms have comparable shapes in terms of direct wave polarities and amplitudes at all three components and close S-P times. Often earthquake catalogues have improved epicentral locations obtained through relocation techniques that help to ensure accurate selection of EGFs. The best pairs are chosen based on close location, preferable with overlapping error location ellipses, and on high (≥0.6) waveform cross-correlation coefficients (Viegas et al., 2010). Mori et al. (2003) noted that the EGF time deconvolution

method started to break down when using earthquake pairs with hypocentral separation larger than ~1.400 km, for M4–M5 earthquakes in California recorded at 10 km to 50 km. Hutchings and Wu (1990) found high waveform cross-correlation for earthquake pairs with hypocentral separation less than 1 km to 3 km, depending on the recording site geology, for M2–M3 Californian earthquakes with similar focal mechanisms, recorded at 3 km to 33 km, for frequencies up to 10 Hz (see Figure 13). Hutchings (1987) investigated spectral similarity for the same events as Hutchings and Wu (1990) and found high coherency (>0.8) for event separations less than 1.5 km. Note that the location uncertainty also plays a role in determining the maximum event separation for which waveform cross-correlation is high. Data with larger location uncertainty will show larger event separation. The event-separation distances can be larger when using coda waves instead of direct waves, because of the averaging properties of coda waves. Mayeda et al. (2007) estimated a limit inter-event separation of 25 km for regional ~M4 earthquakes in California recorded at ~1 km to 220 km. Viegas (2009) estimated an event separation of 750 m for local M2 earthquakes recorded at 4 km to 10 km using coda waves. Comparing the difference in dimension between the two coda-wave studies, we see that the scaling relationship holds.

After the initial selection of EGF earthquake pairs, further constraints can be imposed to assure the adequacy of the EGF earthquake. Viegas et al. (2010) suggested several constraints to improve accuracy obtained with the EGF method. Viegas et al. found that: a clear source pulse in the time domain should be obtained; the corner frequency of the larger earthquake should be well within the frequency band limits of the spectral ratio, so that the fit converges; the corner frequency of the EGF earthquake should be well within the frequency band limits of the spectral ratio to be considered; the high-frequency plateau of the spectral ratio should be well defined; the difference between the low and high frequency plateaus of the spectral ratio should be large enough to be distinguished from spectral modulations; and the normalized-variance of the fit has preferably a parabola shape for a sequence of fixed f_{c1} values, with the minimum variance corresponding to the best fit.

Selecting an EGF that is well recorded at several stations, in order to provide a good azimuthal coverage of the source, is also preferable, so that no bias is introduced by source propagation and directivity effects.

4.2 Source parameters

Once the long-period level of the displacement spectra and the corner frequency or source pulse duration (or rise time) are estimated, the source parameters can be estimated.

4.2.1 Seismic moment and moment magnitude

The scalar seismic moment, M_0, is calculated from the long-period part of the displacement spectrum, following Aki and Richards (2002),

$$M_0 = \frac{4\pi\rho(x)^{1/2}\rho(x')^{1/2}c(x)^{1/2}c(x')^{5/2}R\,\Omega_0}{FU_{\phi\theta}}, \tag{29}$$

where c is the velocity of the wave of interest (α for P wave; and β for S wave), R the hypocentral distance, F the free-surface parameter (F = 2), and $U_{\phi\theta}$ the mean radiation pattern, with $U_{\phi\theta}$ = 0.52 for P waves and $U_{\phi\theta}$ = 0.63 for S waves (Aki and Richards, 2002).

Moment magnitude, M_w, is frequently estimated from the seismic moment using the Hanks and Kanamori (1979) relationship

$$M_w = \frac{2}{3}\log_{10} M_0 - 6.04 \qquad (\text{in N.m}) . \tag{30}$$

4.2.2 Fault radius and stress drop

In earthquake-source parameters studies, it is common to assume a circular fault model. Such a model seems to work well for small to moderate earthquakes, for which the fault dimension correlates well with the rise time. However, the model seems to break down for large earthquakes, in which the fault width is limited by the seismogenic depth and the fault length becomes several times larger. There are several circular source models from which to estimate fault radius, r, from the corner frequency, f_c. The most commonly used are Brune (1970), Sato and Hirasawa (1973), and Madariaga (1976) and are represented by

$$r_B = \frac{2.34c}{2\pi f_c}, \qquad r_{SH} = \frac{Cc}{2\pi f_c}, \qquad r_M = \frac{k\beta}{f_c}, \tag{31}$$

where the index letters in the radius correspond to the model's authors. C and k are constants related to the rupture velocity v_r (C = 1.5 for P waves and C = 1.9 for S waves, k = 0.32 for P waves and k = 0.21 for S waves, assuming $v_r = 0.9\beta$). All three source models implicitly assume a constant subsonic rupture velocity. Brune's static solution model was developed for S waves and later adapted to P waves. Sato and Hirasawa (1973) and Madariaga (1976) models are dynamic solutions using stopping phases. Brune's model radii are approximately 1.76 times larger than Madariaga's radii ,with Sato and Hirasawa radii lying in between. Depending on the source model used, stress drop estimates will differ up to 5.5 times.

Boatwright (1980) proposed a circular rupture model that relates source radius to the source pulse duration, τ, using P waves,

$$r_{Bt} = \frac{v_r \tau}{2\left(1 - \frac{v_r \sin\theta}{\alpha}\right)}, \tag{32}$$

where θ is the take-off angle, assumed to have an average value of 0.64. The dependence on the take-off angle comes from rupture directivity effects. Tomic et al. (2009) found that this model is suitable for P waves but is not consistent with a Madariaga source model for S waves. Viegas et al. (2010) proposed to convert S waves source pulse duration, τ, to corner frequency, using $f_c = 2/\ \pi\tau$ (Lay and Wallace, 1995) and then estimate the fault radius using Madariaga's solution.

Rupture directivity makes the relative duration and amplitude of the source pulse dependent on the recording-station location relative to the fault-plane orientation. The source pulse increases in amplitude and decreases in duration if the rupture propagates towards that station, but it will decrease in amplitude and increase in duration if the rupture propagates away from that station. Sometimes, fault rupture can happen bilaterally, adding complexity to the solution and making it more difficult to distinguish the rupture direction and identify the fault plane.

The static stress released by faulting — that is, the static stress drop, $\Delta\sigma$ — is usually determined from the seismic moment and source radius using Eshelby's (1957) circular static crack solution,

$$\Delta\sigma = \frac{7}{16}\frac{M_0}{r^3}\,. \tag{33}$$

Depending on the source model used, stress-drop estimates can vary by a factor of 5.5, with the Madariaga's (1976) source model 5.5 larger than Brune's (1970), and Sato and Hirasawa's (1973) located between the two.

4.2.3 Radiated energy

The radiated energy of small earthquakes is a particularly difficult parameter to calculate, because it uses the high-frequency portion of the source spectrum. Radiated energy, E_S, is commonly calculated from the integral over the velocity squared source spectra, following Boatwright and Fletcher (1984),

$$E_S = \frac{4\pi\rho\, cR^2 \left\langle U_{\phi\theta} \right\rangle^2}{F^2 U_{\phi\theta}^2} \times 2\int_{f_1}^{f_2} \left|\dot{\Omega}(f)\right|^2 df \tag{34}$$

where $\left|\dot{\Omega}(f)\right|$ is the Fourier velocity amplitude spectrum, f_1 and f_2 are the integration limits, and $\langle U_{\phi\theta}\rangle$ is the rms radiation pattern. When the earthquake focal mechanism is not known, which is often the case, $\langle U_{\phi\theta}\rangle = U_{\phi\theta}$ is assumed. Taking advantage of the EGF method, the spectral ratio can be used to correct for propagation path and site response effects. The velocity spectrum is obtained by differentiation of the EGF spectral ratio, after setting the long-period level of the spectral ratio equal to the long-period level of the displacement spectrum. The energy is calculated from $f_1 = f_c/10$ to $f_2 = 10f_c$ to obtain at least 90% of the total radiated energy (Ide and

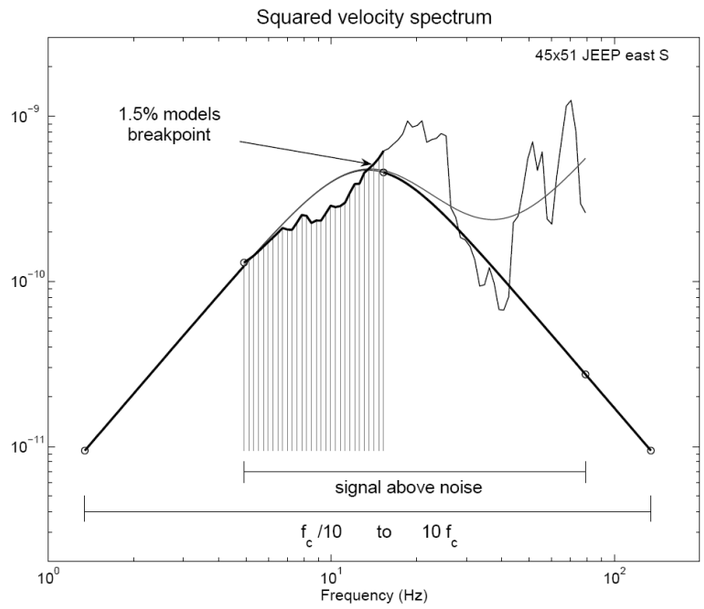

Fig. 10. Illustration of radiated energy calculation. Energy is calculated from the squared spectral ratio. Real data is used between two cut-off frequencies, and model data is used for the remaining frequency band up until a decade above and below the corner frequency. Low frequency cut-off is set for signal to noise ratio above 3. The high frequency cut-off is set when the ratio of the EGF fit model to the individual fit model is above 1.5% (from Viegas et al., 2010).

Beroza, 2001). The available bandwidth does not always reach one or both of those limiting frequencies, so a modeled spectral ratio is used to fill the gaps. The EGF spectral ratio contains two corner frequencies and starts diverging from a ω^2 source model (Brune, 1970) in the vicinity of the smaller earthquake corner frequency. To avoid this distortion at high frequencies, Viegas et al. (2010) use the data spectral ratio exclusively until a certain cut-off frequency is reached, and then use a ω^2 source model for the remaining frequency interval. They set the cut-off frequency to the point where the modeled spectral ratio starts diverging from the modeled ω^2 source by more than 1.5% (Figure 10). Lower-magnitude earthquakes, with corner frequencies closer to the limiting maximum frequency, have a larger energy contribution from the model to fill the high-frequency gap. Earthquakes deconvolved by EGF earthquakes with close magnitudes, and thus close corner frequencies, also have a large model contribution to the energy estimate. The total energy radiated by an earthquake is calculated by summing the contributions of P and S wave energies (Ide et al., 2003).

4.3 Solving for attenuation

Attenuation is often characterized by Q, the frequency-independent attenuation quality factor. Q is usually calculated from modeling the source displacement spectrum with a theoretical source spectrum such as Brune's (1970) (equation 26) and solving for Ω_0, f_c and Q. Ω_0, is very stable and well determined within a factor of 2, but there are several combinations of f_c and Q that fit the spectra equally well. That is, there is a tradeoff between f_c and Q, and any of the combinations provide an optimal fit. Hough et al. (1991) found a way to avoid this caveat by using the corner frequencies calculated from the EGF deconvolution to constrain the source spectrum model when solving for Q. Then, using the obtained Q, Hough et al. (1991) estimated the corner frequencies of other earthquakes that shared common source-station paths, but could not be analyzed using the EGF method. They found the fits were just slightly poorer than the ones obtained solving for Q and f_c simultaneously. Viegas (2011) also used a fixed corner frequency derived from the EGF method and fitted the individual instrument-corrected displacement-spectra using Equation (24a), solving for Q and Ω_0 for all source-station paths. Figure 11 shows an example of Viegas' (2011) EGF analysis applied to the 2010 Germantown, Maryland, USA, M3.4 mainshock and M2.1 aftershock (EGF) pair, and subsequent individual spectrum fitting to obtain Q constrained by the EGF results. It can be seen that the recording site-response observable in the individual spectra was removed by the EGF deconvolution and is no longer observable in the spectral ratio. f_c estimates from fitting the individual spectrum would be biased by the site effects at this station.

Hough (1997) expanded Hough et al.'s (1991) method to determine Q using EGF constrained f_c's, by determining the common source-station attenuation parameter through simultaneously inverting several clustered EGF pairs. This expanded method was called Multiple Empirical Green's Function (MEGF) and has been adopted by other authors with minimal changes (e.g., Hough et al., 1999; Prejean and Ellsworth 2001; Ide et al., 2003; Imanishi and Ellsworth, 2005). Because it simultaneously uses several pairs, it better constrains the attenuation estimate, since the outliers are down-weighed by the most common average properties.

Another common approach to estimating attenuation is to estimate the necessary correction needed to flatten the individual source spectra of an effective impulsive point source EGF, for which the corner frequency is outside the frequency band (e.g., Viegas et al., 2010).

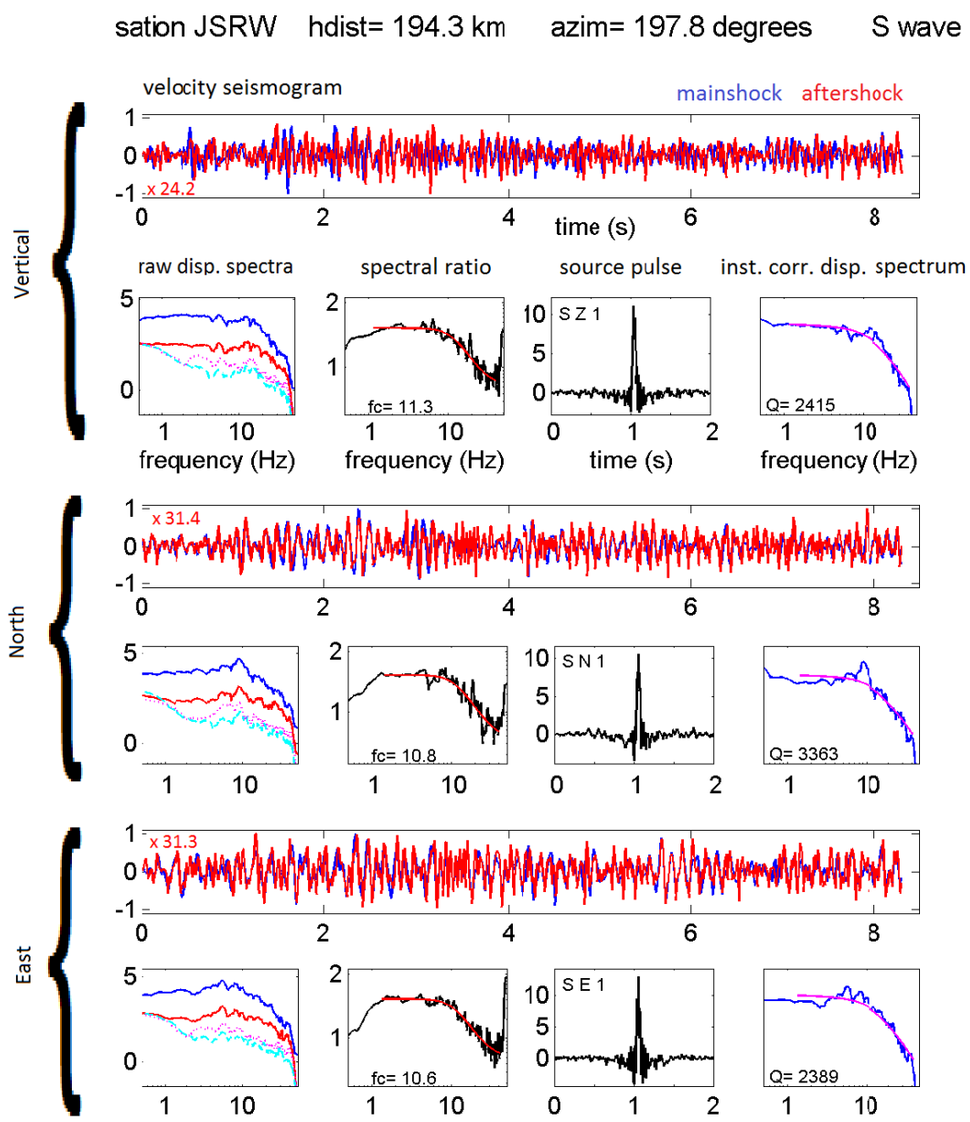

Fig. 11. EGF spectral-ratio-fit analysis. Example of the EGF spectral-ratio-fit analysis at station JSRW (S waves). *Top horizontal panel:* S wave raw velocity seismograms of the 2010 Germantown, Maryland, USA, M3.4 mainshock (blue) and M2.1 aftershock (red). The red number on the plot indicates the multiplication factor applied to the aftershock record to match the amplitude of the mainshock. *Left panel:* Calculated displacement spectra of the seismograms in bottom panel, after integration and instrument correction. The full lines correspond to wave signal, the dotted lines to pre-P noise. *Second panel from left:* Best fit (red) of the EGF spectral ratio (black). The bottom value indicates the best-fit corner frequency. *Third panel from left:* Obtained earthquake source time function. Top left characters correspond to (1) P or S wave, (2) vertical (Z), North (N) or East (E) components, and (3) good (1) or bad (0) fit quality. *Right panel:* Best fit (magenta) of the instrumented corrected displacement spectrum (blue). The bottom value indicates the best-fit attenuation quality factor obtained with the fixed best-fit corner frequency. The panels sequence is repeated three times, one for each component (from Viegas, 2011).

As mentioned in a previous section, Andrews (1986), Boatwright et al. (1991), Prieto et al. (2004), and others used an iterative process to simultaneously solve for source and attenuation terms when dealing with large datasets.

4.4 Increased source resolution with better data and better methods

In the last two decades, we have witnessed a vast improvement in data quality, with the development of borehole acquisition systems and the exponential decrease in computer memory cost, which have enabled the storing of high sampling-rate data. Simultaneously, the use of EGF methods to estimate source parameters of small-to-moderate earthquakes has become more popular, and better attenuation corrections have been conducted. All in all, better data associated with better methods has resulted in better constrained source

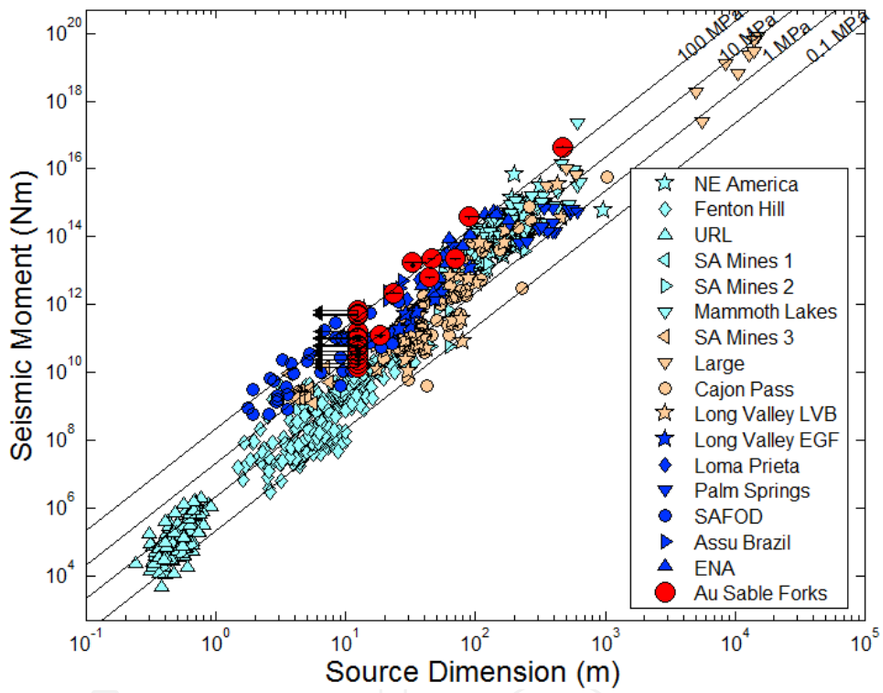

Fig. 12. Global compilation of seismic moment versus source radius, color coded by method used or data type. Dark blue and red indicates EGF methods, peach indicates slip inversion methods or deep borehole data, and light blue indicates individual fitting methods. Viegas et al. (2010) results are shown in red circles. Arrows indicate radii smaller than the maximum resolution threshold. Diagonal lines indicate constant stress drop. (from Viegas et al., 2010, adapted from Abercrombie and Leary, 1993). Data points are: NE America (Boatwright 1994), Fenton Hill (Fehler & Phillips, 1991), URL (Gibowicz et al., 1991), S. A Mines 1 (McGarr et al., 1990), S. A Mines 2 (Spottiswoode and McGarr, 1975), Mammoth Lakes (Archuleta et al., 1982), S. A. Mines 3 (Yamada et al., 2007), Large (compilation of Abercrombie and Rice, 2005, Table 5: Dreger and Helmberger 1991, Mori 1996, Hough and Dreger 1995, Ji et al. 2002, Venkataraman et al. 2000, Wald 1995, Wald and Heaton 1994, Wald et al. 1996, Wald et al. 1991), Cajon Pass (Abercrombie, 1995), Long Valley (Ide et al., 2003, individual and EGF studies), Loma Prieta (Hough et al., 1991), Palm Springs (Mori and Frankel 1990), SAFOD (Imanishi and Ellsworth, 2005), Açu Brazil (Tomic et al., 2009), ENA (Xie et al., 1991; Li et al., 1995; Shi et al., 1998), Au Sable Forks (Viegas et al., 2010).

parameters. An overview of the improvement in source resolution with improved methods and data is illustrated in Figure 12, which is a compilation of earthquake source dimension estimates obtained with various methods. We see in Figure 12 that all stress drop values from EGF methods are above 1 MPa. It seems that with increasing data quality and more accurate methods, stress drop estimates are getting higher—a trend particularly apparent for small earthquakes (<M3). A good example is the Long Valley, CA (Ide et al., 2003) study, showing EGF stress drops that are higher than the individually estimated stress drops.

5. Strong ground-motion synthesis

5.1 EGFs for synthesizing strong ground motion

The use of EGFs in strong ground-motion synthesis has to be qualified not only for high frequencies but for low frequencies as well. Most recordings of small earthquakes are band limited by cultural noise or instrument response, and do not include frequencies below about 0.5 Hz, so that full broadband use of EGFs is not generally possible. This is the frequency range where near-field terms are important for source studies and strong ground-motion synthesis. However, it has long been recognized that synthetic seismograms can be accurately calculated for frequencies < 0.5 Hz in areas where the geology is well known. Often, tomographic inversion for velocity structure provides the basic information necessary to accurately synthesize low-frequency seismograms (Gök and Hutchings, 2004). Thus, there is a convenient match between synthetic Green's functions, which can be accurately calculated for frequencies at which geology can be well known (and can include the near-field wave-propagation effects that are difficult to record)—and EGFs, which record the high frequencies for which the geology is not well known (and for which far-field arrivals are more important). Merging the two frequency bands provides a broadband simulation: synthetic Green's functions can be used for frequencies 0.0 to about 0.5 Hz, and EGFs can generally be used for frequencies from about 0.5 to 25.0 Hz (or higher for stable continental interiors). This covers the frequency range of engineering interest.

5.1.1 Source-event parameters

Earthquakes provide the recordings that are typically used as EGFs. Knowing the source parameters of these earthquakes is critical for correctly including their recordings in mathematical computations. Important source parameters include the hypocentral location, moment, source corner frequency, stress drop, and focal mechanism solution. Moment and source corner frequency, which are particularly important parameters, can be the most difficult to estimate. Virtually all EGF synthesis methods add up or scale EGFs based upon their moment, and the amplitudes of synthesized records are linearly dependent upon these estimates. Similarly, many EGF methods scale records with stress drops or deconvolve out the source event spectra, and these computations are directly dependent upon the source corner-frequency estimate. Typically, a source model (e.g., a Brune source or Boatwright source) is used to characterize the source corner frequency and moment,, and from this the source dimensions and stress drop is derived. (Calculating hypocentral location and focal mechanism solutions are not discussed here. Earthquakes are typically recorded by local or regional networks, and these parameters can be well constrained).

5.1.2 Interpolation of EGFs

Typically, EGFs from recordings of small earthquakes are not necessarily on the faults to be modeled. Moreover, if they are on the fault to be modeled, they are not necessarily recorded

from all locations along a fault, or share the same focal mechanism solution. As a consequence, to represent all the fault elements, it is necessary to interpolate EGFs and modify their focal mechanism solution. Hutchings and Wu (1990), researching the spatial dependence of EGFs, found that the variability in ground motion caused by differences in source location and/or focal mechanism solutions are much less than those caused by the site response. Hutchings (1991), Hutchings (1994), and Jarpe and Kasameyer (1996) also found that interpolation for different source locations along a fault works quite well. Wossner et al. (2002) found that the number of EGFs affects the amplitude of synthesized seismograms. They found that amplitudes in the synthesized records for frequencies higher than the source corner frequency generally tend to be higher for records that use a single EGF interpolated over the fault, and they achieved more stable and reliable results if at least five EGFs were used. In synthesis, we have the option of correcting for different focal mechanism solutions, but Hutchings and Wu (1990) and Jarpe and Kasameyer (1996) found that for high frequencies, this correction does not improve the synthesis. Interpolation is performed by correcting for attenuation, geometrical spreading, and P-wave and S-wave arrival times resulting from differences in source distances, as discussed in Hutchings and Wu (1990). Figure 13 shows cross-correlation values for events with spatial separations up to 5 km and with similar focal mechanism solutions. It can be seen that the best cross-correlation coefficients are obtained when both small event separation and common focal mechanisms are verified.

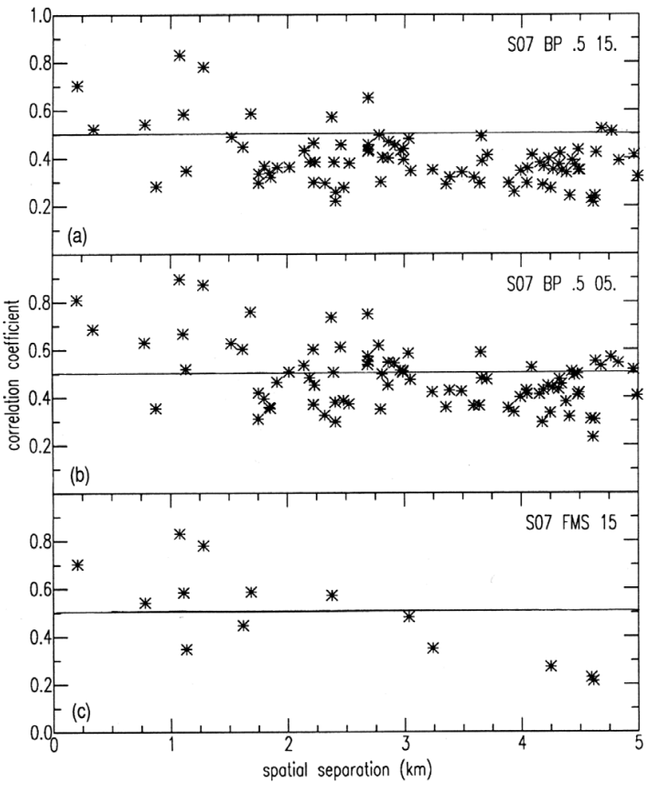

Fig. 13. Cross-correlation values of events with spatial separations up to 5 km and with similar focal mechanism solutions, at several frequency bands: (a) 0.5 Hz to 15.0 Hz; (b) 0.5 Hz to 5.0 Hz; **(c)** 0.5 Hz to 15.0 Hz for which variations in the focal solution angles strike, slip, and dip less than 15 degrees. (from Hutchings and Wu, 1991).

5.1.3 Scaling relations

A significant issue for strong ground-motion synthesis with EGFs is how to properly scale small earthquakes to model a large earthquake. Most strong ground-motion synthesis methods depend upon a scaling relation to determine how many EGFs to use in synthesizing a larger earthquake. If constant stress-drop scaling is assumed between small and larger earthquakes, and the earthquakes follow a non-constant scaling relationship, small earthquakes will systematically have a larger moment for the same apparent stress drop as large earthquakes, and thus fewer EGFs will be needed to add up to the moment of the larger event. Therefore, the assumed scaling relation directly affects the amplitude of the synthesized seismograms. Hutchings (1991 and 1994) proposed that if one follows the representation relation in synthesis and uses EGFs that are effectively impulsive point sources, then one only needs to use the number of EGS that add up to the moment of the larger earthquake. This avoids scaling relations (see equations 20 and 21).

5.1.4 Deconvolution to obtain EGFs

Often, small earthquakes have moments greater than the threshold necessary to effectively be impulsive point sources. One can use the output of source parameter studies to deconvolve out the finite source from the recordings to create EGFs. Generally, investigators confine this approach to events with magnitude < 4.0 to minimize finite source effects and keep the basic assumption of the Brune source model. The Brune source has zero phase shifts, such that in the deconvolution, only the amplitude spectra are affected. There is no apparent noncausal effect in the time series due to the deconvolution. Figure 14 shows several recordings that have been corrected to effectively provide impulsive point, earthquake source-event recordings (EGFs). The time series are in acceleration, and their displacement spectra are shown. That the spectra are not flat after the deconvolution is assumed to result from the effects of attenuation and site response (*fmax* effect).

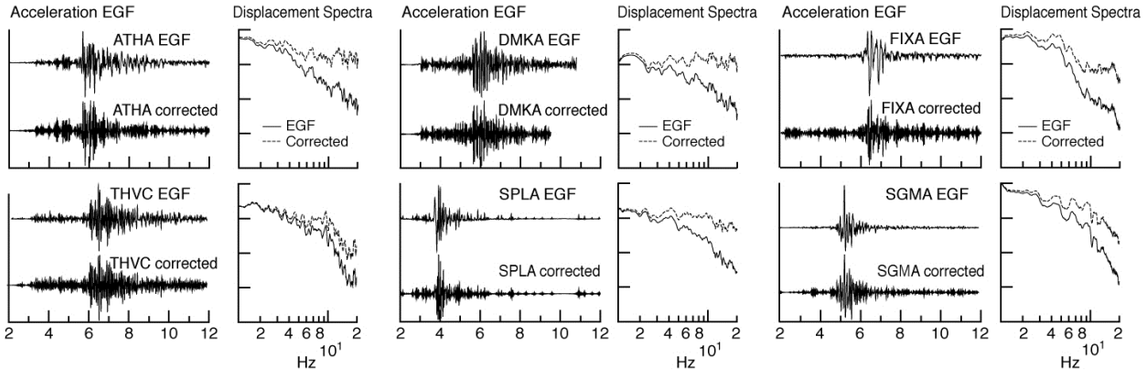

Fig. 14. Several recordings that have been corrected to effectively provide impulsive point earthquake sources. The time series are in acceleration, and their displacement spectra are shown. The fall-off at higher frequencies of the corrected spectra is due to attenuation and site effects.

5.1.5 Empirical Green's Functions merged with synthetic Green's functions

Since EGFs are recordings of actual earthquakes, they are band limited by cultural noise and instrument response. One way to overcome this band limitation is to augment these

recordings by synthetic Green's functions from ground-motion synthesis. The basic premise in combining empirical and synthetic Green's functions is that each offers the best accuracy over particular frequency bands. EGF's, as noted above, are more accurate at high frequencies, at which wherein geologic inhomogeneities are not well modeled, and the synthetic Green's functions are more accurate at lower frequencies, at which EGFs do not have sufficient energy. The overlap is in the range from 0.2 to 1.0 Hz. In this range, the geology can be modeled with some accuracy, and EGFs have sufficient energy to be well recorded.

There are limitations to the mathematical solution for Green's functions. First, analytical Green's functions cannot account for small-scale geologic inhomogeneities, and as a result cannot reasonably model ground motion for frequencies much greater than about ~1 Hz. Given this limitation, geologic inhomogeneities in the spatial dimension of ~3 km or smaller cannot be modeled. Second, inaccurate estimates of attenuation and scattering properties can significantly affect synthesized frequency content. Hutchings and Wu (1990) presented a means for providing site response functions to synthetic Green's functions that improves the reliability of synthetic Green's functions.

5.1.6 Empirically constrained stochastic EGFs

We can create synthetic high-frequency Green's functions with Gaussian white noise shaped by an envelope function and modified by attenuation, geometrical spreading, and kappa functions. This approach has been described by Boore (1983 and 2003). Regional propagation information obtained by regression on recorded seismicity (Malagnini and Herrmann, 2000) and site-specific K obtained from geotechnical information (Akinci et al., 2001) can be used to modify the shape of the source spectra—so that the stochastic Green's functions have the averaged wave propagation characteristics of the region, and site-specific information when possible. In this sense, Green's functions are empirically derived. These Green's functions with impulsive point dislocation sources can be used in the representation relation to calculate seismograms using equations (11) or (13). (Low frequencies (< ~1.0 Hz) might better be computed by synthetic seismograms and merged, as discussed in the previous section.) One approach proposed by Hutchings et al. (2005) is to use synthetic Green's function for low frequencies, EGFs for middle frequencies, and stochastic Green's functions for very high frequencies. Stochastic Green's functions can be expressed as

$$e_n(X,t) = P(t) * D(R,t) * R(t)\,, \tag{35}$$

where *P(t)* is a stochastic time series with a specified envelope shape and duration, and with a Fourier amplitude spectrum from an impulsive point shear dislocation. D(R,t) is the propagation effect resulting from geometrical spreading and attenuation determined by inversion on background seismicity, such as developed by Herrmann and Malagnini (1996). *R(t)* is the site response from either recorded data or site-specific kappa obtained from geotechnical data (Akinci et al., 2001).

The Fourier amplitude spectrum of the Green's function displacement can be expressed as

$$\left|E_n(M_0, R, \omega)\right| = \left|P_n(M_0, R, \omega)\right| \cdot D(R, \omega) \cdot R(\omega)\,. \tag{36}$$

The far-field displacement spectrum for seismic P-waves from a point shear dislocation source in a homogeneous whole space (Aki and Richards, 2003, eqs. 4.93 – 4.95) is

$$\left|P_P(M_0, R, \omega)\right| = \frac{\mu A \bar{s}(x') U_{\phi\theta}^P}{4\pi R^\gamma \rho(x)^{1/2} \rho(x')^{1/2} \alpha(x)^{1/2} \alpha(x')^{5/2}}, \tag{37}$$

where the primed terms are values at the source and the unprimed are values at the receiver. $\bar{s}(x')$ is the average displacement of the point dislocation, A is the fault area, and μ is the rigidity. These three terms together are the seismic moment of the stochastic Green's function. We only specify the moment of the point source and not these individual values. The spectrum is flat. Similarly, for S-waves,

$$\left|P_S(M_0, R, \omega)\right| = \frac{M_o^e U_{\phi\theta}^S}{4\pi R^\gamma \rho(x)^{1/2} \rho(x')^{1/2} \beta(x)^{1/2} \beta(x')^{5/2}}, \tag{38}$$

The average radiation values ($U_{\phi\theta}^P$ and $U_{\phi\theta}^S$) of P, SH, and SV waves are used, and α, β, and ρ are the P- and S-wave velocities and density of the medium at the surface or on the fault. R^γ is the geometrical spreading, where R is the hypocentral distance and γ is a geometrical spreading factor, generally between 0.9 and 1.1, and is determined from regression of regional seismicity as discussed below.

5.2 Source models

Strong ground-motion synthesis with EGFs has been the subject of research and application since 1978. It has intrigued researchers because such a synthesis provides seismograms that appear very realistic in frequency content, duration, and energy distribution. Our primary interest in this section is in using the EGF method for engineering purposes. For that reason, the frequency band of interest is about 0.5 to 25.0 Hz. Basically, the idea of using a recording of an earthquake for the wave propagation of the synthesis model is the same for all approaches, though there are differences regarding the number and size of EGFs used, as well as regarding the scaling relation between the EGFs and the larger event. Some investigators use only one EGF for the entire synthesis and assume that the wave propagation characteristics are the same from all portions of a fault. Others use several EGFs to try to account for differences in wave propagation. There are never enough small earthquakes to provide EGFs for all portions of a fault, so the assumption of slowly varying Green's functions for source locations along the fault is typically made. Most methods use an interpolation scheme to fill out the fault with EGFs. To be mathematically accurate, the EGFs must have the same focal mechanism as the larger event to be modeled. Since this is not generally true, an interpolation for differences in focal mechanism solutions and an estimation of the error involved should be included in the results—as discussed in the previous section.

The greatest difference between methods is in the source function assumed. There are five basic classes of source functions: point source, stochastic, kinematic, quasi-dynamic, and dynamic. There are further classifications of synthesized models, such as target spectrum, composite source, and continuous source summation—but these are secondary classifications, since they can have a stochastic, kinematic, or quasi-dynamic source. Point-source models generally are forced to fit a target spectrum without any phase information. Stochastic methods generally have time delays that are randomly chosen from a distribution, so they represent a finite fault in that sense, but there is no coherency that might result from a rupture

process. Kinematic modeling is generally interpreted to mean that the contribution from each portion of a fault is specifically prescribed. Generally, this includes some form of rupture propagation, rise time, and slip distribution. Quasi-dynamic modeling generally involves earthquake models that are consistent with the physics of the rupture process and attempt to simulate the dynamic character of rupture. Thus, they must be consistent with the elastodynamic equations of seismology and fracture energy, and be consistent with a physical understanding of how earthquakes rupture, as well as the laboratory experiments, numerical modeling results, and field observations involved in earthquake processes. Dynamic modeling is a full calculation of the state of stress as a function of time and displacements, and stress release depends upon a friction law and material prosperities. Dynamic modeling has not previously been applied with EGFs and is not discussed here.
Size differences in the EGFs that are used affect the source time function. Those that use events larger than point sources to obtain EGFs are basically obtaining part of their source function from the EGF itself. Some methods discussed here use synthetic Green's functions, but EGFs could just as well have been used, so they are also examined. Similarly, any of the EGF synthesis methods could equally as well use synthetic records as Green's functions instead of EGFs. All the approaches follow the representation relation in some form (equations 11 and 13), and this relation is used as a common basis for comparison between methods.

5.2.1 Point source

Point-source approaches make no assumption about how earthquakes rupture. Rather, they add up EGFs with no phase information or force them to fit a target spectra. This is the basic approach first presented by Joyner and Boore (1986), where an original seismogram (EGF) spectra is modified to fit the target spectra by iteratively shaping in the frequency and time domain.

5.2.2 Composite source modeling

Most EGF methods utilize a composite source summation. This approach has its roots in research that described large events as composite of smaller "subevents" (Wyss and Brune, 1967; Trifunac and Brune, 1970; Kanamori and Stewart, 1976). However, these are generally confined to three or four subevents. Inversion studies indicate that subevents may be large patches of high-energy release along the rupture surface (Hartzell and Heaton, 1983, 1986; Hartzell and Iida, 1990), and deconvolution studies reveal multiple rupture events within a larger event's source time functions (Lay et al., 1982; Lynnes and Lay, 1988). These studies generally indicate that there are three or four subevents in most ruptures, which does not support a composite earthquake model in which tens or even hundreds of events are repeatedly summed to create a synthesis of a larger event. Nevertheless, many authors have been successful in synthesizing observed seismograms with the composite earthquake model. This approach can be summarized as (equation 14)

$$u_n(X,t) = \sum_{j=1}^{\eta} \kappa_j e_n\left(X, t' - \tau_j\right)_j , \tag{39}$$

where κ_j is a scaling factor for Green's functions, η is the number of times small events are added to create the synthetic seismogram, and τ_j are determined from the rupture model.

Joyner and Boore (1986) proposed one form of the composite model: they assumed κ was constant and that only one EGF was used, and described EGFs that have corner frequencies in the observable frequency range, i.e., they used a composite source model. They then developed constraints on the numbers of composite sources necessary to create the desired time series of a larger earthquake and showed that if constant stress-drop scaling and Brune spectra were applied,

$$\eta = \left(\frac{M_0}{M_0^e}\right)^{\frac{4}{3}} \quad \text{and} \quad \kappa = \left(\frac{M_0}{M_0^e}\right)^{\frac{1}{3}}. \tag{40}$$

This results from requiring the moment of the small earthquake to be scaled and added to be that of the large earthquake, and requiring the high frequency fall-off of the small earthquake, above its corner frequency, to match the amplitude of the larger earthquake. They showed that if τ_j were evenly distributed, this approach results in amplitude deficiencies in the spectrum near the corner frequency of the simulated event, and holes in the spectrum. If we examine Equation (39) in view of the representation relation (equations 13 and 14), the Joyner and Boore approach is basically a Haskell (1964) rupture, which assumes equal amplitude of slip with constant rise time and constant rupture velocity throughout the rupture surface. Note that the Haskell rupture model has been shown to be deficient in frequencies near the corner frequency and have spectral holes in the high frequency (Hutchings, 1994).

5.2.3 Stochastic source modeling

Many investigators take the approach of modeling a large earthquake as the sum of smaller earthquakes that are added together stochastically. That is, there is a probability distribution that describes the time delays in the summation. For example Joyner and Boore (1986), as discussed in the previous section, assumed an even probability distribution for time delays in the summation. That is, τ_j in Equation (39) is evenly distributed between 0.0 and the duration of the earthquake. The distribution replicates rupture in time and space, but there is no coherency in the rupture that would occur during a real earthquake. This approach has been termed the single-stage approach, because there is only one time-delay probability distribution.

Wennerberg (1990) showed that the deficiencies in the spectra observed by Joyner and Boore (1986) were caused by the transform of a uniform probability density having a periodic set of zeros. From Equation (20), the scaling can also be described by the cosine function's periodicity, where the τ's are equal. To overcome these problems, Wennerberg proposed a summation scheme in two stages. The first is a probability distribution of the event summation, and the second is a distribution about each of the first,

$$u_n(X,t) = \sum_{i=1}^{\eta}\sum_{j=1}^{\gamma} \kappa_j e_n(X, t_i' - \tau_i^r - \tau_k^s)_i \,. \tag{41}$$

Wennerberg also kept κ constant. It is apparent that Equation (41) is in the same form as Equation (13). Equation (41) has the characteristics of a more complicated rupture, with the first stage representing rupture along the fault and the second stage representing rise time. However, there is no coherency to the rupture. Also, Wennerberg assumed that the spectra

of the large event fits the omega-squared Brune source model, which is not necessarily true for the near-source region, where earthquake damage usually occurs.

It is instructive to compare the frequency-domain solutions of equations (18) and (19) to equations (39) and (41). Equation (18) is the frequency domain solution to Equation (14). Equation (18) is derived assuming an impulsive point-source event, so comparisons are only precisely valid below the corner frequency of source events used by Joyner and Boore or Wennerberg, but higher frequencies essentially have the same result. Had the phase spectrum in Equation (19) been a probability distribution in τ, only one EGF been used, and the scaling factors κ_j been constant, then Equation (14) would be identical to Wennerberg's Equation (1). If the probability distribution were described as a uniform probability, it would be identical to Equation (A2) in Joyner and Boore's (1986) Appendix. Thus, the main difference between stochastic modeling and actual rupture of earthquakes is that the phase delays associated with rupture are approximated by probability distributions. However, it is critical what distributions are used, and their implications need to be identified. Also, using only one EGF assumes that the amplitude and phase spectrum of the EGF are constant over the fault rupture area. Although there is substantial evidence that the amplitude spectrum is fairly constant for different locations of EGFs, assuming that the phase spectrum remains constant is fairly dubious.

5.2.4 Kinematic source modeling

Kinematic modeling involves simulating the actual rupture process by prescribing what happens at all points along a simulated fault rupture. Typically, rupture velocity, rise time, and slip distribution are prescribed. Irikura (1986) has developed one of the most widely used methods for synthesizing ground motion with EGFs—a kinematic, composite source model approach. He applied the relation

$$u_n(X,t) = \sum_{i=1}^{M} \left(\frac{r}{r_i} \right) F\left(t - t_i'\right) * e_n(X,t) , \tag{42}$$

where

$$F(t) = \delta(t) + \frac{1}{n} \sum_{j=1}^{n\left(\sqrt{M}-1\right)} \delta\left[t - \frac{(j-1)\tau}{n\left(\sqrt{M}-1\right)} \right], \tag{43}$$

and where M describes a finite fault with N rows times N columns, M=N×N, with the number of subevents determined by the ratio of the source parameters of the large event being synthesized to the small event being used as an EGF. Only one EGF is used. r and r_i are the hypocentral distances of the EGF earthquake and of the i^{th} subfault element to the recording site, respectively. This is the interpolation scheme used by Irikura to provide an effective EGF at each source area. t'_i is the sum time delay from the rupture starting point to the i^{th} element and that from the i^{th} element to the site. τ is the rise time of the source rupture process of the large event. n is an appropriate integer number to shift fictitious periodicity $\tau/(N-1)$ into a high frequency out of the range of interest. The primed terms refer to descriptions on the source, and $*$ is the convolution operator. $F(t)$, addressed as a filtering function, is a series of delays in summation of the Green's function over the rise time of the larger event. Substituting Equation (43) into (42), we have

$$u_n(X,t) = \sum_{i=1}^{M} \frac{r}{r_i} e_n(X, t - t_i^{'}) + \sum_{i=1}^{M} \sum_{j=1}^{N} \frac{r}{n r_i} e_n(X, t - t_i^{'} - t_j^{'}) \,, \tag{44}$$

where

$$t_j^{'} = \frac{(j-1)\tau}{N} \quad \text{and} \quad N = n\left(\sqrt{M} - 1\right). \tag{45}$$

Equation (44) is in the form of a single-stage approach added to a two-stage approach, as discussed in the composite source section above (equations 39 and 41, respectively). Equation (44) is also in the same form as Equation (11), so it is a solution of the representation relation. In the spirit of Equation (10) through Equation (15), where the Green's function is separate from the source function and the interpolation scheme for EGFs is not shown as part of the equation, $\hat{S}^{'}(t^{'})$ of Equation (11) can be expressed with Irikura's filter function as

$$\hat{S}^{'}(t^{'}) = \frac{M_{0i}^{e}}{\mu_i A_i} \left[\delta(t - t_i) + \frac{1}{n} \sum_{j=1}^{N} \delta\left(t - t_i - t_j\right) \right], \tag{46}$$

where M_{0i}^{e}, μ_i, and A_i are as described for equations (11) through (15). To examine the slip function of the representation relation expressed in Equation (10), it is important to keep in mind that the retrieved source function is a relative source obtained through deconvolution, so that

$$\hat{S}(t^{'}) = \hat{S}^{'}(t^{'}) * S_e(t^{'}) \,, \tag{47}$$

where $S_e(t')$ is the source function of the EGF event and $*$ is the convolution operator. If the EGF is from an impulsive point-source event, i.e., at frequencies below its source corner frequency (so that the EGF source function is a step function), then $\hat{S}(t^{'})$ of Equation (10) can be expressed as

$$\hat{S}(t^{'}) = \frac{M_{0i}^{e}}{\mu_i A_i} \left[H(t - t_i) + \frac{1}{n} \sum_{j=1}^{N} H\left(t - t_i - t_j\right) \right] \tag{48}$$

where $H(t')$ is the step function and is the form of Equation (12). As discussed below, the key issue for the slip function is how one describes the phase delays t_i and t_j. Irikura describes these as constant throughout the fault, and consequently they describe a constant velocity rupture front with a step at the arrival time of the rupture front plus a ramp slip over the rise time. Except for the initial step, this is a Haskell rupture.

Hartzell et al. (1999) proposed a kinematic model based upon a fractal distribution of subevents,

$$u_n(X,t) = \left[\sum_{k=1}^{L} S_{km}(t) * \sum_{j=1}^{M_k} S_{ok}(t) * \sum_{i=1}^{N_k} \frac{r_0}{r_{ij}} \left(\frac{\Delta\sigma_{ij}}{\Delta\sigma_0} \right) \delta\left(t - t_{sij} - t_{rij}\right) \right] * e(x,y,t)_{ij} \tag{49}$$

where $e(x,y,t)$ is the displacement for a small event as discussed above (EGF). It could be from an EGF or a calculated subevent. L is the number of different subevent spatial sizes, M_k is the number of subevents with size k, and N_k is the number of the smallest subevents needed to fill the fault area of subevent jk. r_0 is the distance from the subevent to the station, and r_{ij} scales this for geometrical spreading due to actual distance from actual subevent. $(\Delta\sigma_{ij}/\Delta\sigma_0)$ scales the stress drop at each subevent relative to that of the Green's function. The spectrum of the source function $S_{ij}(f)$ is that of the ratio of a Brune spectra between the EGF to that of the subevent. This source model has no theoretical relationship between rupture parameters and the elastodynamic equation of motion. The value at each element is arbitrarily applied. However, the similarity to the representation relation is apparent: the terms in the square bracket are the source time function of the representation relation (Equation 11 and following).

5.2.5 Quasi-dynamic modeling

Quasi-dynamic modeling generally involves earthquake models that are consistent with the physics of the rupture process and attempt to simulate the dynamic character of rupture. Several investigators have approached strong ground-motion synthesis with quasi-dynamic rupture models, including Boatwright (1981), Hartzell (1982), Heaton (1982), Papageiorgiou and Aki (1983), Spudich and Frazier (1984), Cohee et al. (1991), Hutchings (1991 and 1994), and Guatteri et al. (2003). Quasi-dynamic source models allow for model combinations of rupture parameters that have not yet occurred in nature. Bounds on input parameters are based on physical understanding and naturally bound the synthesized ground motions.

5.2.5.1 Hutchings' method

Hutchings (1991, 1994, and 2007) used the Kostrov (1964) slip function to describe slip at a point. The Kostrov slip function was derived from the analytical solution for rupture of a circular crack in a homogeneous medium (Buridge and Willis, 1969),

$$K\left(X,t^{'}\right)=\frac{0.81\Delta\sigma\beta}{\mu}\sqrt{t^{'2}-\frac{\chi_i^2}{v_r^2}}\ , \tag{50}$$

where X_i^2 is the position vector from the hypocenter, t' is relative to the origin time of the earthquake, v_r is the rupture velocity, β is the shear wave velocity, 0.81 is a constant used for v_r equal to 0.9β, μ is rigidity, and $\Delta\sigma$ is stress drop. This expression does not include healing or termination of the slip. Hutchings transformed the Kostrov slip function to be relative to element time and added healing to the slip process. The Kostrov slip function at an element becomes

$$S(t^{'})_i=\frac{0.81\Delta\sigma_i\beta_i}{\mu_i}\sqrt{t_i^{'2}+2t_r^i t_i^{'}}\otimes H(t^{'})\qquad t_i^{'}\le\tau_i\ , \tag{51}$$

where t'_i is zero at the arrival time of a rupture front, so that $t'_i = t' - t'_r$, and t'_r is the rupture time from the hypocenter, χ/v_r, in Equation (50). τ_i is the rise time at the i^{th} element, and $\otimes H(t')$ is the deconvolution with the step function. The slip at an element follows Equation (51) from the arrival time of the rupture front to its rise time. Hutchings modeled the rise time as the time for termination of slip due to a stress pulse propagating back into the fault area after rupture has terminated at an edge. This is the result

determined by Kostrov and Das (1990) from dynamic modeling. Now, t'_r places a rupture distance dependence on Equation (49), and for long faults it causes $S(t')_i$ to increase with spatial separation from the hypocenter. To constrain this, t'_r is limited to be equal to or less than the rupture time to the nearest edge but not less than 1.0 sec. Hutchings equates this limiting value to an "asperity termination" of fault rupture and a departure from a pure crack solution for an extended rupture. This is consistent with the observation of a slip pulse as identified by Heaton (1990).

Other features of this quasi-dynamic model include rigidity diminishing at the same rate as the stress drop near the surface. This has two effects: first, reducing the rigidity results in very little moment contribution for rupture near the surface; second, the commensurate diminishing of stress drop results in significant displacements (although not significantly seismogenic) at the surface. Further, as a result of these near-surface rupture effects, Hutchings does not allow a slip healing-phase to be generated for the termination of rupture at or near the surface.

Investigators often use knowledge about how earthquakes rupture to estimate bounds of possible rupture parameters that may have been identified prior to an earthquake. Rupture parameters are selected by a Monte Carlo method using a triangular distribution between limits. The limits of input parameters will naturally bound the range of synthesized ground motions. Also, because input parameters are correlated through a physical model, combinations that cannot occur in nature are excluded. Certainly, a major area of research in the future will be identifying the physical limits to input parameters in order to get the maximum physical range of ground motion possible (Bommer et al., 2004).

Fault shapes, slip distributions, and asperities are constrained to have the character of previously occurring earthquakes, but are not determined by regression on these parameters. Slip distributions of previous earthquakes show that rectangular ruptures generally occur on faults that rupture through the entire crust (Scholz, 1980), whereas earthquakes that terminate before reaching the surface of the entire crustal thickness have an elliptical shape (Hartzell and Iida 1990; Hartzell and Heaton 1983, 1986; Wald and Graves 2001). The definition of an asperity as defined by Somerville et al. (1999) provides guidelines for asperities. Somerville et al. used inversion results, primarily from Hartzell or Wald and Graves, to characterize the slip distribution of an asperity as having a slip amplitude greater than 1.5 times the overall average slip amplitude. From regression with all their data and results from Wells and Coppersmith (1994), Somerville calculates asperities to occupy 22% of the total rupture area and account for 44% of the total slip.

Rupture velocity is allowed to vary from 0.75 to 1.0 times the shear-wave velocity, as derived from dynamic rupture modeling (Das and Kostrov, 1990, and many others). Healing velocity is 0.8 and 1.0 times the rupture velocity, lying roughly between the Raleigh wave velocity and the shear wave velocity, as observed in dynamic rupture modeling. Stress drop in Equation (49) is a dependent variable derived from the Kostrov slip function. In this derivation, stress drop is that which results in a strain discontinuity and displacement on the fault, and results in seismic radiation. It is equivalent to the Orowan stress drop (Orowan, 1960). Stress drop is constrained to diminish near the surface of the earth due to the lithostatic load (about 30 MPa at 1.7 km depth). Figure 15 shows an example of synthetic waveforms and derived spectra obtained with the Hutchings' method that best model the rupture of the M6 1997 Colfiorito, Italy, earthquake (Scognamiglio and Hutchings, 2009).

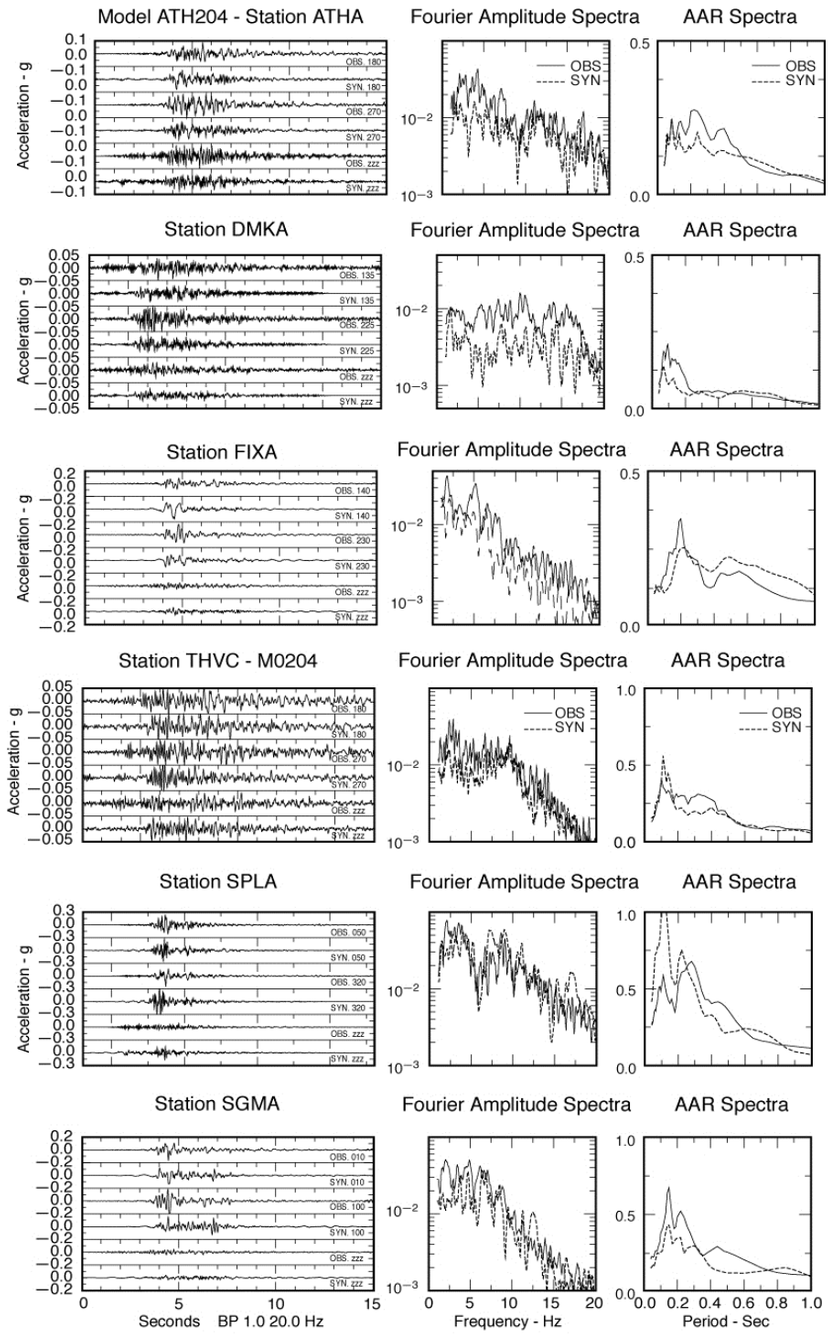

Fig. 15. Example of modeling the rupture of the M6 1997 Colfiorito, Italy, earthquake using the Hutchings' method. The fit between the observed (solid lines) and synthesized (dashed lines) seismograms (*left panels*), displacement Fourier spectra (*center panels*) and acceleration response spectra (*right panels*) are shown for all available stations for the preferred rupture model. Notice that the basic characteristics of the synthesized seismograms (SYN) closely match the observed seismograms (OBS). In particular, the basic waveforms, durations, and frequency content match well. The frequency content is evident from the Fourier amplitude and ARR spectra (from Scognamiglio and Hutchings, 2009).

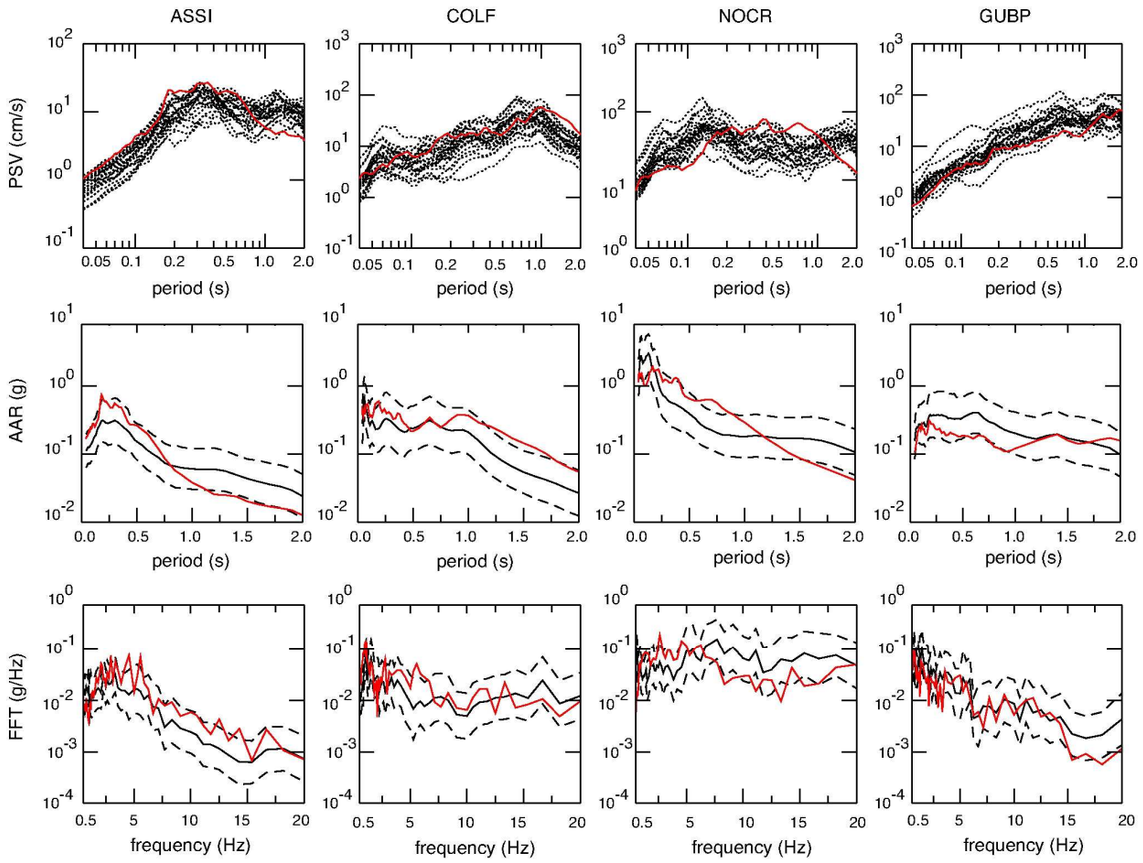

Fig. 16. Calculated twenty-three scenarios using "tight" constraints (dotted lines) in the smaller source volume where the M6 1997 Colfiorito, Italy earthquake is thought to have occurred at the available recording stations, as well as those observed from the actual earthquake (red curves). *Top panels:* PVR calculated for all models. *Middle and bottom pannels*: mean (thick solid line) and plus and minus standard deviation of the distribution (thick dashed lines) of acceleration response spectra (AAR) and Fourier spectra (FFT) for all models that includes epistemic and aleatory uncertainty. (from Scognamiglio and Hutchings, 2009)

Obviously, when rupture parameters are varied, they combine to give a distribution of ground-motion amplitudes. In studying the effects of source parameter changes on acceleration time series and Fourier amplitude spectra, Wossner et al. (2002) found that hypocenter location greatly affects near-source stations due to a directivity effect, that different fault plane geometries significantly affect rise-time distribution and thus amplitude and frequency content of signal, and that variations in rupture and healing velocities can cause up to a factor-of-five difference in time-series amplitudes. These variations are caused by parameters that generally cannot be known prior to an earthquake. If parameters can be constrained, then the distribution should narrow. Scognamiglio and Hutchings (2007) showed that if some parameters are known in advance, then the distribution can be narrowed. The test for a physically based approach to ground-motion prediction is that when the parameters are narrowed, the distribution should still contain what actually happened. Figure 16 shows that for the M=6.0 Colfiorito, Italy earthquake, this is true. The recorded data are within the one-standard-deviation value of the synthesized suite of

spectra, with the shapes of the synthesized spectra matching (in general) the shapes of the observed spectra, thus indicating the prediction capability of the method.

6. Strong ground motion prediction and application to seismic hazard analysis

The main goal of strong ground-motion prediction is to model ground motion near sources of potentially damaging earthquakes. It is this near-source region, within about two-fault–lengths' distance, wherein damage from earthquakes principally occurs. It is also within this distance range that finite rupture can significantly influence the character of ground motion. Therefore, a principal concern of strong ground-motion synthesis is to model the rupture process of large earthquakes. In addition, near-source ground-motion synthesis should also accurately account for the complexity of wave propagation. Unfortunately, EGF's do not include the effects of material nonlinearity caused either by modular damping and reduction or by loss of effective stress (liquefaction), and therefore the synthesized ground motion is for linear response. Typically, non-linear soil modeling is used to convert this to potential non-linear response (Heuze et al., 1994).

Making accurate earthquake predictions requires a physical model for earthquakes. One approach is to use quasi-dynamic source models as we have discussed above to generate rupture scenarios that span the variability of potential ground motion in a predictive situation. The basic premise is that fifty years of strong motion records is insufficient to capture all possible ranges of site and propagation path conditions, rupture processes, and spatial geometric relationships between source and site. Predicting future earthquake scenarios is necessary; models that have little or no physical base but have been tested and adjusted to fit available observations can only "predict" what happened in the past, which is "describing" not "predicting" at all. The ultimate solution for modeling earthquakes would be dynamic solutions that satisfy both elastodynamic equations and fracture mechanics, and that have known elastic constants and constituent relations for faulting processes. Estimates of these parameters for the fault zone carry large uncertainties and require several poorly bounded assumptions. The resultant uncertainties in computations limit their usefulness in better understanding of the earthquake process and in providing bounds for kinematic rupture models.

The basic premises of quasi-dynamic modeling for purposes of ground-motion prediction are:

1. Accurate synthesis of recorded ground motions for a particular fault rupture scenario, sufficient for engineering purposes, is possible;
2. A general description of the rupture is sufficient for synthesizing realistic ground motions;
3. The rupture characteristics of a fault can be constrained in advance by interpreting physical properties such as geologic structure, seismicity, and regional tectonics;
4. The range of possible fault-rupture scenarios is narrow enough to functionally constrain the range of strong ground motion predictions; and
5. A discrete set of rupture scenarios is sufficient, for engineering purposes, to span the infinite combinations possible from a given range of rupture parameters.

An important corollary for testing this approach is that if a scenario earthquake matches the seismograms from an actual earthquake, then the rupture parameters of that scenario are close to what actually happened. Pavic et al. (2000), for example, made an assessment of uncertainties and confidence level in the selection of rupture parameters.

Historically, strong ground-motion prediction has generally taken one of two paths: probabilistic or deterministic. Following Cornell (1968), probabilistic seismic hazard analyses (PSHA) require: (1) an interpretation of seismic sources that constitute a hazard to a particular site, from which the distance of an earthquake to the site can be determined; (2) an interpretation of earthquake recurrence for each source; and (3) an evaluation of ground-motion attenuation for the region. The ground-motion attenuation relationships are simple functions of earthquake magnitude and source-site distance (and in some cases a few additional source parameters), and are empirically derived from the strong-motion database recorded from past earthquakes worldwide. Finally (4), given the input evaluations, the PSHA method integrates over all values of the variables and produces an estimate of the mean yearly frequency of exceedance of ground-motion amplitude at the site (i.e., a hazard curve). Figure 17 illustrates the components of a probabilistic hazard study.

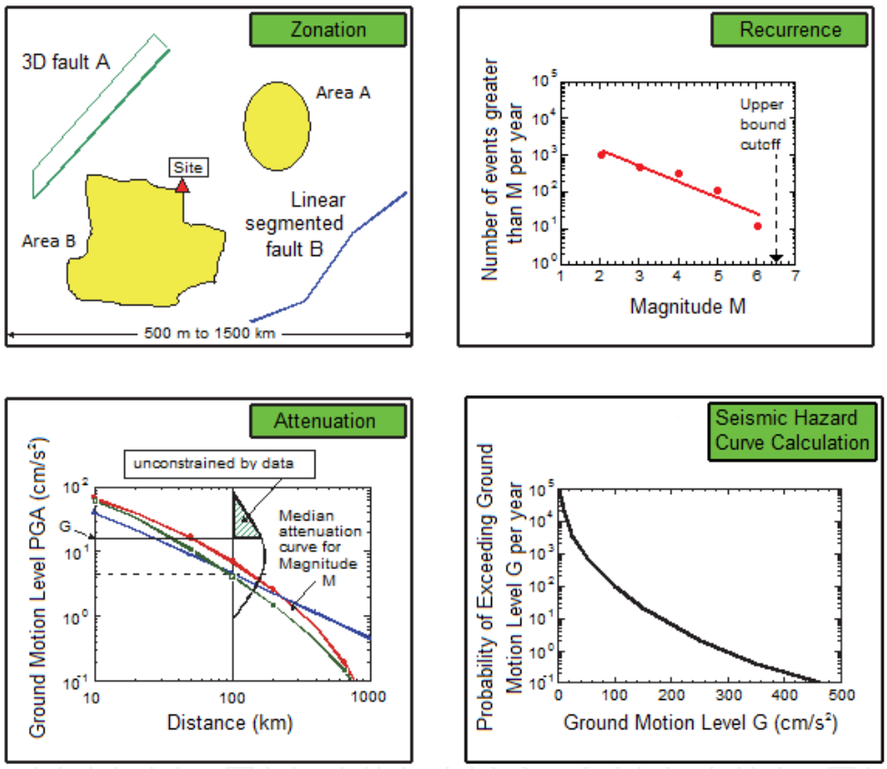

Fig. 17. Components of a probabilistic seismic hazard (PSHA) study. *Top left*: Representation of the source region for PSHA. *Top right*: Typical example of a Gutenberg-Richter b-value relationship. *Bottom left*: Distribution of attenuation relations along with the log normal distribution. *Bottom right*: Seismic hazard curve.

Both earthquake source models and ground-motion attenuation relationships are subject to significant uncertainties, which are expressed as probability distributions (giving an estimate of the median and standard deviation) on earthquake occurrence rates and on the ground-motion relationships. The uncertainty in a ground-motion relationship arises from the variability in source characteristics among events of the same size in the strong-motion database, and from the different earth structures through which the seismic waves from the events propagated. In PSHA studies, this is considered aleatory uncertainty, the uncertainty

due to inherent randomness of the process. Current PSHA studies are based upon the ergodic assumption that the randomness in space from several sources is the same as the randomness in time from the same source (Anderson and Brune, 1999). With this ergodic assumption, correlation between the ground motion and the specific source, path, and site is lost, thereby leading to potentially higher total uncertainty in hazard estimates than if each earthquake-source release of energy were individually propagated to the site of interest. There is also an attempt to model epistemic uncertainty, the uncertainty in knowledge about earthquake processes. This refers to factors such as strike, dip, slip vector, etc., that could further reduce aleatory uncertainty if they were known and included as regression parameters.

Alternatively, a deterministic approach identifies significant faults or source zones and establishes the Maximum Possible Earthquake (MPE) for PSHA; Design Operating Earthquake (DOE), essentially the mean of PSHA; and the Operating Basis Earthquake (OBE), maximum during lifetime of facility. Deterministic hazard studies have had the problem of identifying the appropriate source for each earthquake and their likelihood of occurrence, and PSHA has had the problem of insufficient historical data and accurately accounting for epistemic uncertainty with respect to the source and propagation of strong ground motion.

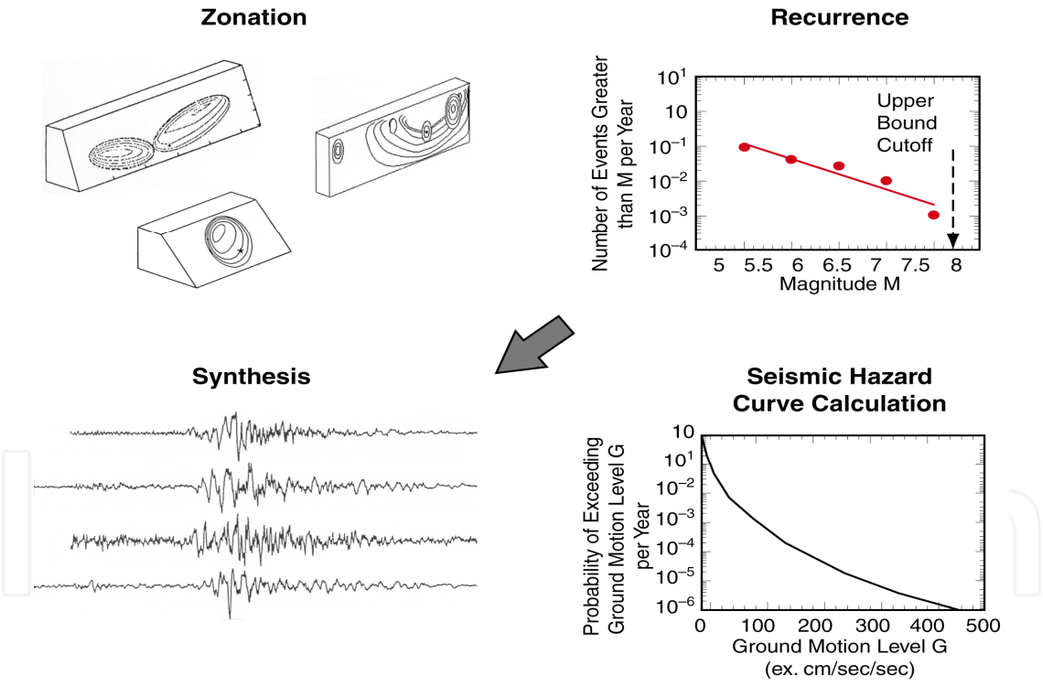

Fig. 18. Components of a physics-based PSHA study. *Top left*: Fault rupture scenarios represent the source region. *Top right*: Typical example of a Gutenberg-Richter b-value relationship. *Bottom left*: Synthesized ground motions. *Bottom right*: Seismic hazard curve for a particular synthesized ground motion.

We can incorporate the combination of deterministic studies by calculating the actual earthquake rupture and recorded ground motion relevant to a particular site, and incorporating this into PSHA studies by replacing the use of attenuation relations. The

output from this PSHA approach is a library of source- and site-specific ground-motion time series that would comprise a sample of all the earthquakes that could affect a site during its design life. The uncertainty of the PSHA is defined by bounds on the physical parameters that go into the computation of ground motion rather than having an unbounded PSHA developed from unbound shapes to probability distributions. The library of seismograms is used to either develop hazard curves of traditional engineering parameters, in the form of the annual probability of exceedance, or used directly in developing risk estimates. This alternative approach is illustrated in Figure 18. It replaces the aleatory uncertainty that current PSHA studies estimate by regression of empirical parameters from the worldwide database, with epistemic uncertainty as to what specific sources may actually do at specific sites. Figure 19 illustrates the hazard curve that would result from such an approach. This approach is essentially that recommended by the Southern California Earthquake Center, Phase III study (Filed et al., 2000), which concluded that complex propagation effects unique to earthquake-rupture/site combinations result in uncertainties that require replacing the standard empirical-regression method with one based on a more physics-based approach to ground-motion modeling. This approach has further been endorsed by the National Research Council (2003). A sound framework with which to implement this approach on a large scale has been proposed by Field et al. (2003).

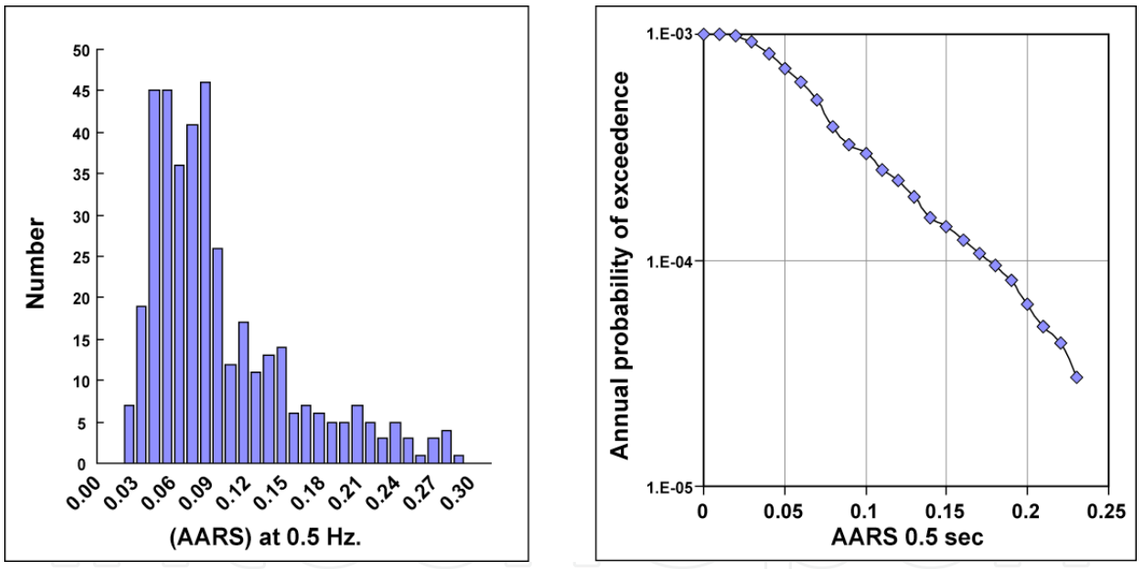

Fig. 19. Hazard Curve .*Left*: Histogram of the number of occurrence of each value of the hazard parameter. *Right*: Cumulative number of occurrences exceeding each hazard value normalized by year.

7. References

Abercrombie, R. E. (1995). Earthquake source scaling relationship from –1 to 5 ML using seismograms recorded at 2.5-km depth, *J. Geophys. Res.*, Vol. 100, pp. 24015-24036.

Abercrombie, R. E. (1998). A summary of attenuation measurements from borehole recordings of earthquakes: The 10 Hz transition problem. *Pure and Appl. Geophys.*, Vol. 153, pp. 475-487.

Abercrombie, R. E., and P. C. Leary (1993). Source parameters of small earthquakes recorded at 2.5 km depth, Cajon Pass, southern California: implications for earthquake scaling, *Geophys. Res. Lett.*, Vol. 20, pp. 1511-1514.

Abercrombie, R. E., and J. R. Rice (2005). Can observations of earthquake scaling constrain slip weakening? *Geophys. J. Int.*, Vol. 162, pp. 406-424, doi: 10.1111/j.1365-246X.2005.02579.x.

Abercrombie, R. E., W. Walter, and R. Gök (2012). Comparison of Direct and Coda Wave stress drop measurements for the Wells, Nevada, earthquake sequence, (in prep).

Abrahamson, N.A., and B. A. Bolt (1987). Array Analysis and Synthesis Mapping of Strong Ground Motion, in *Strong Motion Synthetics*, edited by B.A. Bolt, pp. 55-90, Academic Press, Orlando, Florida, U.S.A.

Aki, K. (1967). Scaling law of seismic spectrum, *J. Geophys. Res.*, Vol. 72, pp. 1217–1231.

Aki, K. and P. G. Richards (2002). *Quantitative Seismology* (2nd Edition), University Science Books, ISBN: ISBN0935702962, 9780935702965, Sausalito, California, U.S.A.

Akinci, A., L. Malagnini, R. B. Herrmann, N. A. Pino, L. Scognamiglio, and H. Eyidogen (2001). High-frequency ground motion in the Erzincan region, Turkey; inferences from small earthquakes, *Bull. Seism. Soc. Am.*, Vol. 91, No. 6, pp. 1446-1455.

Allmann, B. P., and P. M. Shearer (2007). Spatial and temporal stress drop variations in small earthquakes near Parkfield, California, *J. Geophys. Res.*, Vol. 112, No. B4, B04305, doi: 10.1029/2006JB004395.

Allmann, B. P., and P. M. Shearer (2009). Global variations of stress drop for moderate to large earthquakes, *J. Geophys. Res.*, Vol. 114, No. B01310, doi: 10.1029/2008JB005821.

Anderson, J. G. (1986). Implication of attenuation for studies of the earthquake source, in *Earthquake Source Mechanics*, *Geophysical Monograph 37, Maurice Ewing Vol. 6,* S. Das, J. Boatwright, and C. H. Scholz (Editors), pp. 311-318, American Geophysical Union, Washington, D.C., U.S.A.

Anderson, J. G. and J. Brune (1999). Probabilistic seismic hazard analysis without the ergodic assumption. *Seism. Res. Lett*., Vol. 71, No. 1, pp. 19-28.

Anderson, J. G. and S. Hough (1984). A model for the shape of the Fourier amplitude spectra of accelerograms at high frequencies, *Bull. Seism. Soc. Am*., Vol. 74, pp. 1969-1994.

Andrews, D. J. (1986). Objective determination of source parameters and similarity of earthquakes of different size, in *Earthquake Source Mechanics, Geophysical Monograph 37, Maurice Ewing Vol. 6,* S. Das, J. Boatwright, and C. H. Scholz (Editors), pp. 259-268, American Geophysical Union, Washington, D.C., U.S.A.

Archuleta, R. J. (1986). Downhole recordings of seismic radiation, in *Earthquake Source Mechanics, Geophysical Monograph 37*, *Maurice Ewing Vol. 6,* S. Das, J. Boatwright and C. H. Scholz (Editors), pp. 319-329, American Geophysical Union, Washington, D.C., U.S.A.

Archuleta, R. J., E. Cranswick, C. Mueller, and P. Spudich (1982). Source parameters of the 1980 Mammoth Lakes, California, earthquake sequence, *J. Geophys. Res.*, Vol. 87, pp. 4595-4607.

Aster, R.C. and P.M. Shearer (1991). High-frequency borehole seismograms recorded in the San Jacinto Fault Zone, Southern California, Part 2. Attenuation and site effects, *Bull. Seismol. Soc. Am.*, Vol. 81, pp. 1081-1100.

Baise, L. G., L. J. Hutchings, and S. D. Glaser (2001). Site Response at Yerba Buena Island, San Francisco Bay from Weak Motion Recordings. *Bollettino Di Geofisica Teorica ed Applicata*, Special Issue on "Site Response Estimate from Observed Ground Motion Data.", Vol. 42, No. 3-4, pp. 219-244.

Bakun, W. H. and C. G. Bufe (1975). Shear-wave attenuation along the San Andreas Fault zone in Central California, *Bull. Seism. Soc. Am.*, Vol. 65, pp. 439-460.

Baltay, A., G. Prieto, and G. Beroza (2010). Radiated seismic energy from coda measurements indicates no scaling in apparent stress with seismic moment, *J. Geophys. Res.*, Vol. 115, No. B8, doi: 10.1029/2009JB006736.

Boatwright, J. (1980). A spectral theory for circular seismic sources: simple estimates of source duration, dynamic stress drop, and radiated energy, *Bull. Seismol. Soc. Am.*, Vol. 70, pp. 1-28.

Boatwright, J. (1981). Quasi-dynamic models of simple earthquake: an application to an aftershock of the 1975 Oroville, California earthquake. *Bull. Seis. Soc. Am.*, Vol. 71, pp. 69-94.

Boatwright, J. (1994). Regional propagation characteristics and source parameters of earthquakes in Eastern North America, *Bull. Seism. Soc. Am.*, Vol. 84, pp. 1-15.

Boatwright, J., and J. B. Fletcher (1984). The partition of radiated energy between *P* and *S* waves, *Bull. Seism. Soc. Am.*, Vol. 74, pp. 361-376.

Boatwright, J., J. B. Fletcher, and T. E. Fumal (1991). A general inversion scheme for source, site, and propagation characteristics using multiply recorded sets of moderate-sized earthquakes, *Bull. Seism. Soc. Am.*, Vol. 81, No. 5, pp. 1754-1782.

Bommer, J. J., N. A. Abrahamson, F. O. Strasser, A. Pecker, P.-Y. Bard, H. Bungum, F. Cotton, D. Fah, F. Sabetta, F. Scherbaum, and J. Studer (2004). The Challenge of Defining Upper Bounds on Earthquake Ground Motion. *Seis. Res. Lett.*, Vol. 75, No. 1, pp. 82-95, doi: 10.1785/gssrl.75.1.82.

Bonilla, L. F., J. H. Steidl, G. T. Lindley, A. G. Tumarkin, and R. J. Archuleta (1997). Site amplification in the San Fernando valley, CA: variability of the site effect estimation using the S-wave coda, and H/V methods, *Bull. Seism. Soc. Am*. Vol. 87, pp. 710-730.

Boore, D. M. (1983). Stochastic simulation of high-frequency ground motions based on seismological models of the radiated spectra, *Bull. Seism. Soc. Am.*, Vol. 73, pp. 1865--1894.

Boore, D. M. (2003). Simulation of ground motion using the stochastic method, *Pure and Applied Geophysics*, Vol. 160, pp. 635-676.

Brune, J. (1970). Tectonic stress and the spectra of seismic shear waves from earthquakes, *J. Geophys. Res.*, Vol. 75, pp. 4997-5009.

Burridge, R. and J. Willis (1969). The self-similar problem of the expanding elliptical crack in an anisotropic solid, *Proc. Cambridge Phil. Soc.,* Vol. 66, pp. 443-468.

Cohee, B. P., P. G. Somerville, and N. A. Abrahamson (1991). Simulated Ground Motions for Hypothesized Mw= 8 Subduction Earthquakes in Washington and Oregon. *Bull. Seism. Soc. Am.*, Vol. 81, pp. 28-56.

Cornell, C. A. (1968). Engineering Seismic Risk Analysis, *Bull. Seism. Soc. Am.*, Vol. 58, pp. 1583-1606.

Das, S., and B. V. Kostrov (1990). Inversion for seismic slip rate history and distribution with stabilizing constraints: Application to the 1986 Andreanof Islands Earthquakes. *Journal of Geophysical Research,* Vol. 95, No. B5, pp. 6899–6913, doi: 10.1029/ 90JB00701, ISSN: 0148-0227.

Dreger, D., and D. Helmberger (1991). Source parameters of the Sierra Madre earthquake from regional and local body waves, *Geophys. Res. Lett.,* Vol. 18, pp. 2015–2018.

Dreger, D. S. (2003). TDMT_INV: Time Domain Seismic Moment Tensor INVersion, *International Handbook of Earthquake and Engineering Seismology,* Vol. 81B, p 1627.

Eshelby, J. D. (1957). The determination of the elastic field of an ellipsoidal inclusion and related problems, *Proc. Roy. Soc. Lond., A,* Vol. 241, pp. 376-396.

Fehler, M. and W. S. Phillips (1991). Simultaneous inversion for *Q* and source parameters of microearthquakes accompanying hydraulic fracturing in granitic rock, *Bull. Seism. Soc. Am,* Vol. 81, pp. 553–575.

Field, E. H. and K. H. Jacob (1993). The theoretical response of sedimentary layers to ambient seismic noise. *Geophys. Res. Lett.*, Vol. 20, No. 24, pp. 2925-2928.

Field, E.H. and the Phase II Working Group (2000). Accounting for site effects in probabilistic seismic hazard analyses of southern California: Overview of the SCEC Phase II Reeport, *Bull. Seism. Soc. Am.*, Vol. 90, pp. S1-S31.

Field, E.H., T. H. Jordan, and C. A. Cornell (2003). OpenSHA: a developing community-modeling environment for seismic hazard analysis, *Seism. Res. Lett*., Vol. 74, No. 4, pp. 406–419.

Frankel, A. (1982). Precursors to a magnitude 4.8 earthquake in the Virgin Islands: spatial clustering of small earthquakes, anomalous focal mechanisms, and earthquake doublets, *Bull. Seism. Soc. Am.,* Vol. 72, pp. 1277-1294.

Frankel, A. (1991). High-frequency spectral falloff of earthquakes, fractal dimension of complex rupture, b value, and the scaling of strength on faults, *J. Geophys. Res*., Vol. 96, pp. 6291 – 6302.

Frankel, A. and H. Kanamori (1983). Determination of rupture duration and stress drop from earthquakes in southern California, *Bull. Seism. Soc. Am.* Vol. 73, pp. 1527-1551.

Frankel, A., J. Fletcher, F. L. Vernon, L. Haar, J. Berger, T. Hanks, and J. Brune (1986). Rupture characteristics and tomographic source imaging of *M L* ~ 3 earthquakes near Anza, southern California, *J. Geophys. Res.,* Vol. 91, pp. 12633-12650.

Frankel, A. and L. Wennerberg (1989). Microearthquake spectra from the Anza, California, seismic network: site response and source scaling, Bull. Seis. Soc. Am. 79, 581-609.

Gibowicz, S.J., R. P. Young, S. Talebi and D. J. Rawlence (1991). Source parameters of seismic events at the Underground Research Laboratory in Manitoba, Canada: scaling relations for events with moment magnitude smaller than -2, *Bull. seism. Soc. Am.,* Vol. 81, pp. 1157–1182.

Gök, R., K. Doan and L. Hutchings (2003). Source parameters and scaling relations for aftershocks of the 1999 Marmara earthquakes, *EOS, Trans. Am. Geophy. Union*.

Gök, R. and L. Hutchings (2004). Broadband Green's Functions for the 1999 Marmara Earthquake Region Based on Local Earthquake Recordings, in *American Geophysical Union, Western Pacific Geophysics Meeting*, Honolulu, Hawaii, 16-20 August 2004.

Guatteri, M. P., M. Mai, G. C. Beroza and J. Boatwright (2003). Strong Ground-motion Prediction from Stochastic-Dynamic Source Models. *Bull. Seis. Soc. Am*., Vol. 93, pp. 301-313.

Hanks, T. (1977). Earthquake stress drops, ambient tectonic stresses and stresses that drive plate motions, *Pure and Applied Geophysics*, Vol. 115, No. 1-2, pp. 441-458, doi: 10.1007/BF01637120.

Hanks, T. (1982). *fmax*, *Bull. Seism. Soc. Am*., Vol. 72, pp. 1869-1879.

Hanks, T. and H. Kanamori (1979). A moment magnitude scale. *J. Geophys. Res*., Vol. 84, pp. 2348-2350.

Hanksson, E., T.-L. Teng, and T. L. Henyey (1987). Results from a 1500 m deep, three-level downhole seismometer array: site response, low Q values and *fmax*, *Bull. Seism. Soc. Am.,* Vol. *77*, pp. 1883-1904.

Hartzell, S. (1978). Earthquake aftershocks as Green's functions, *Geophys. Res. Lett*., Vol. 5, pp. 1-4.

Hartzell, S. (1982). Simulation of ground accelerations for May 1980 Mammoth Lakes, California, earthquakes, *Bull. Seis. Soc. Am*., Vol. 72, pp. 2381-2387.

Hartzell, S. and T. H. Heaton (1983). Inversion of strong ground motion and teleseismic waveform data for the fault rupture history of the 1979 Imperial Valley, California earthquake, *Bull. Seismol. Soc Am*., Vol. 73, pp. 1553-1583.

Hartzell, S. and T. H. Heaton (1986). Rupture history of the 1984 Morgan Hill, California, earthquake from the inversion of strong motion records, *Bull. Seism. Soc Am*., Vol. 76, pp. 649-674.

Hartzell, S. and M. Iida (1990). Source complexity of the 1987 Whittier Narrows, California, Earthquake from the inversion of strong motion records, *J. Geophys. Res.,* Vol. 95, pp. 12475-12485.

Hartzell, S., S. Harmsen, A. Frankel and S. Larsen (1999). Calculation of Broadband Time Histories of Ground Motion: Comparison of Methods and Validation using Strong-Ground Motion from the 1994 Northridge Earthquake. *Bull. Seism. Soc. Am*., Vol. 89, pp. 1484-1504.

Haskell, N. A. (1964). Total energy spectral density elastic of wave radiation from propagating faults, *Bull. Seismo. Soc. Am*., Vol. 54, pp. 1811-184I.

Haskell, N. A. (1966). Total energy and energy spectral density of elastic wave radiation from propagating faults, II, *Bull. Seism. Soc. Am*., Vol. 56, pp. 125–140.

Heaton, T. H. (1982). The 1971 San Fernando earthquake: a double event? *Bull. Seism. Soc. Am*., Vol. 72, part A, pp. 2037-2063.

Heaton, T. H. (1990). Evidence for and implications of self-healing pulses of slip in earthquake rupture, *Phys. Earth Planet Int*., Vol. 64, pp. 1-20.

Herrmann, R. B., and L. Malagnini (1996). Absolute ground motion scaling in the New Madrid Seismic Zone, *Seism. Res. Lett.,* Vol. 67, pp. 40.

Heuze, F. E., T. S. Ueng, L. J. Hutchings, S. P. Jarpe, and P. W. Kasameyer (1994). A coupled seismic-geotechnical approach to site-specific strong motion, Soil Dynamics and Earthquake Engineering. 16 (4): 259-272 JUN 1997.

Hough, S. E. (1997). Empirical Green's function analysis: taking the next step, *J. Geophys. Res*., Vol. 102, pp. 5369-5384.

Hough, S. E. , K. Jacob, and P. Filberg (1989). The 11/25/88, M = 6 Saguenay earthquake near Chicontimi, Quebec: evidence for anisotropic wave propagation in northeastern North America, *Geophys. Res. Lett.*, Vol. 16, pp. 645-648.

Hough, S. E., L. Seeber, A. Lerner-Lam, G. Armbruster, and H. Guo (1991). Empirical Green's function analysis of Loma Prieta aftershocks, *Bull. Seism. Soc. Am*., Vol. 81, pp. 1737-1753.

Hough, S. E., and D. S. Dreger (1995). Source parameters of the 23 April 1992 M 6.1 Joshua Tree, California, earthquake and its aftershocks; empirical Green's function analysis of GEOS and TERRAscope data, *Bull. Seism. Soc. Am.,* Vol. 85, pp. 1576–1590.

Hough, S. E., J. M. Lees, and F. Monastero (1999). Attenuation and source properties at the Coso Geothermal Area, California, *Bull. Seism. Soc. Am*., 89(6), 1606-1619.

Hutchings, L. (1987). Modeling near-source earthquake ground motion with empirical Green's functions, Ph.D. Thesis, State University of New York.

Hutchings, L. (1991). Prediction of strong ground motion for the 1989 Loma Prieta earthquake using empirical Green's functions, *Bull. Seism. Soc. Am*., Vol. 81, pp. 88-121.

Hutchings, L. (1994). Kinematic Earthquake Models and Synthesized Ground Motion Using Empirical Green's Functions, *Bull. Seism. Soc. Am.*, Vol. 84, pp. 1028-1050.

Hutchings, L. and F. Wu (1990). Empirical Green's functions from small earthquakes: waveform study of locally recorded aftershocks of the San Fernando earthquake, *J. Geophys. Res.*, Vol. 95, pp. 1187-1214.

Hutchings, L., B. Foxall, P. Kasameyer, S. Larsen, C. Hayek, C. Tyler-Turpin, J. Aquilino, and L. Long (2005). Deep Borehole Instrumentation along San Francisco Bay Bridges: 1996 – 2003 and Strong Ground Motion Synthesis along the San Francisco/Oakland Bay Bridge. Final Report July 15, 2005. Also, annual progress reports. Caltrans contract no. 59A0238. UCRL-TR-2117303.

Hutchings, L., Ioannidou, E., Kalogeras, I., Voulgaris, N., Savy, J., Foxall, W., Scognamiglio, L., and Stavrakakis, G. (2007). A strong motion prediction methodology; application PSHA and the 7 September 1999, M = 6.0 Athens Earthquake, *Geophys. J. Int.*, Vol. 168, pp. 659–680, doi: 10.1111/j.1365-246X.2006.03178.x.

Ide, S., and G. C. Beroza (2001). Does apparent stress vary with earthquake size? *Geophys. Res. Lett.*, Vol. 28, pp. 3349-3352.

Ide, S., G. C. Beroza, S. G. Prejean, and W. L. Ellsworth (2003). Apparent break in earthquake scaling due to path and site effects on deep borehole recordings, *J. Geophys. Res.*, Vol. 108, No. B5, doi:10.1029/2001JB001617.

Imanishi, K., and W. L. Ellsworth, (2006). Source scaling relationships of microearthquakes at Parkfield, CA, determined using the SAFOD pilot hole seismic array, in *Earthquakes: Radiated Energy and the Physics of Faulting, Geophysical Monograph 170*, edited by R.E. Abercrombie, A. McGarr, H. Kanamori and G. Di Toro, pp. 81–90, American Geophysical Union, Washington, D.C., U.S.A.

Irikura, K. (1984). Prediction of strong ground motions using observed seismograms from small events, *Proc. 8th World Conf. on Earthq. Eng.*, Vol. 2, pp. 465-472.

Irikura, K. (1986). Prediction of strong acceleration motion using empirical Green's function. *Proc. 7th Japan Earthq. Eng. Synp.*, pp. 151-156.

Jarpe, S., L. J. Hutchings, T. F. Hauk, and A. F. Shakel (1989). Selected Strong and Weak Motion Data from the Loma Prieta Earthquake Sequence, *Seism. Res. Letters*, Vol. 60, pp. 167-176.

Jarpe, S., and P. K. Kasameyer (1996). Validation of a Methodology for Predicting Broadband Strong Motion Time Histories using Kinematic Rupture Models and Empirical Green's Functions. *Bull. Seism. Soc. Am.*, Vol. 86, pp. 1116-1129.

Ji, C., D. J. Wald, and D. V. Helmberger (2002). Source description of the 1999 Hector Mine, California, earthquake, Part II: Complexity of slip history, *Bull. Seism. Soc. Am.*, Vol. 92, pp. 1208–1226.

Joyner, W. B. and D. M. Boore (1986). On simulating large earthquakes by Green's-function addition of smaller earthquakes, in *Earthquake Source Mechanics, Geophysical Monograph 37, Maurice Ewing Vol. 6,* S. Das, J. Boatwright, and C. H. Scholz (Editors), pp. 269-274, American Geophysical Union, Washington, D.C., U.S.A.

Kanamori, H., and G. S. Stewart (1976). Mode of the strain release along the Gibbs fracture zone, Mid-Atlantic ridge, *Phys. Earth Planet. Int.*, Vol. 11, pp. 312-332.

Kanamori, H., and T. H. Heaton (2000). Microscopic and macroscopic physics of earthquakes, in *Geocomplexity and the Physics of Earthquakes*, *Geophysical Monograph Series* Vol. 120, edited by J. Rundle, D. L. Turcotte and W. Kein, pp. 147-155, American Geophysical Union, Washington, D.C., U.S.A.

Kostrov, B. V. (1964). Self similar problems of propagation of shear cracks, *J. Appl. Math. Mech. (PMM)*, Vol. 28, pp. 1077-1087.

Kostrov, B. V., and S. Das (1988). *Principles of earthquake source mechanics*, in Cambridge Monographs on Mechanics and Applied Mathematics, Cambridge University Press, Cambridge, UK.

Lay, T., H. Kanamori and L. Ruff (1982). The asperity model and the nature of large subduction zone earthquake occurrence, *Earthquake Prediction Research,* Vol. 1, pp. 3-71.

Lay, T., and T. C. Wallace (1995). *Modern Global Seismology*, Academic Press, ISBN: 012732870X, 9780127328706, San Diego, California, U.S.A.

Li, Y., C. Jr. Doll, and M. N. Toksöz (1995). Source characterization and fault plane determination for M_{bLg} = 1.2 to 4.4 earthquakes in the Charlevoix Seismic Zone, Quebec, Canada, *Bull. Seism. Soc. Am.*, Vol. 85, pp. 1604-1621.

Lynnes, C. S. and T. Lay (1988). Source process of the great 1977 Sumba earthquake, *J. Geophys. Res.*, Vol. 93, pp. 13407-13420.

Madariaga, R. (1976). Dynamics of an expanding circular crack, *Bull. Seism. Soc. Am.*, Vol. 66, pp. 639-666.

Malagnini, L., and R. B. Herrmann (2000). Ground motion scaling in the region of the 1997 Umbria-Marche earthquake (Italy), *Bull. Seism. Soc. Am.*, Vol. 90, pp. 1041-1051.

Malin, P.,E., and J. A. Waller (1985). Preliminary results from vertical seismic profiling of Oroville microearthquake S-waves, *Geophys. Res. Lett.*, Vol. 12, No. 3, pp. 137-140

Mayeda, K., and W.R. Walter (1996). Moment, energy, stress drop and source spectra of western United States earthquakes from regional coda envelopes, *J. Geophys. Res.,* Vol. 101, pp. 11195-11208.

Mayeda, K., A. Hofstetter, J. O'Boyle, and W.R. Walter (2003). Stable and transportable regional magnitudes based on coda-derived moment-rate spectra, *Bull. Seism. Soc. Am.*, Vol. 93, pp. 224-239.

Mayeda, K., L. Malagnini, W.R. Walter (2007). A new spectral ratio method using narrow band coda envelopes: Evidence for non-self-similarity in the Hector Mine sequence, *Geophys. Res. Lett.*, Vol. 34, No. L11303, doi:10.1029/2007GL030041.

McGarr, A., (1999). On relating apparent stress to the stress causing earthquake fault slip, *J. Geophys. Res.*, Vol. 104, pp. 3003-3011.

McGarr, A., J. Bicknell, J. Churcher and S. Spottiswoode (1990). Comparison of ground motion from tremors and explosions in deep gold mines, *J. Geophys. Res.,* Vol. 95, pp. 21777–21792.

Mori, J., (1996). Rupture directivity and slip distribution of the M4.3 foreshock to the 1992 Joshua Tree earthquake, southern California, *Bull. Seism. Soc. Am.,* Vol. 86, pp. 805–810.

Mori, J., and A. Frankel (1990). Source parameters for small events associated with the 1986 North Palm Springs, California, earthquake determined using empirical Green functions, *Bull. Seism. Soc. Am.*, Vol. 80, pp. 278-295.

Mori, J., R. E. Abercrombie, and H. Kanamori (2003). Stress drops and radiated energies of aftershocks of the 1994 Northridge, California, earthquake, *J. Geophys. Res.*, Vol. 108, No. B11, 2545, doi: 10.1029/2001JB000474.

Mueller, C. S. (1985). Source pulse enhancement by deconvolution of an empirical Green's function, *Geophys. Res. Let.*, Vol. 12, pp. 33-36.

National Research Council (2003). *Living on an Active Earth: Perspectives on Earthquake Science*, National Academic Press, Washington, D.C

Orowan, E. (1960). Mechanism of seismic faulting, *Geol. Soc. Am. Bull*., 79, 323–345.

Papageorgiou, A.S. and K. Aki (1983). A Specific Barrier Model for the Quantitative Description of Inhomogeneous Faulting and the Prediction of Strong Ground Motion. Part I: Description of the Model, *Bull. Seism. Soc. Am.*, Vol. 73, No. 3, pp. 693-722.

Pasyanos, M.E., D.S. Dreger, and B. Romanowicz (1996). Toward Real-Time Estimation of Regional Moment Tensors, *Bull. Seism. Soc. Am*., Vol. 86, pp. 1255-1269.

Pavic, R., M. G. Koller, P.-Y. Bard, and C. Lacave-Lachet (2000). Ground Motion prediction with the empirical Green's function technique: an assessment of uncertainties and confidence level, *Journal of Seismology*, Vol. 4, pp. 59-77.

Prejean, S. G., and W. L. Ellsworth (2001). Observations of earthquake source parameters at 2 km depth in the Long Valley Caldera, eastern California, *Bull. Seismol. Soc. Am.,* Vol. 91, pp. 165-177.

Prieto, G., P. M. Shearer, F. L. Vernon, and D. Kilb (2004). Earthquake source scaling and self-similarity estimation from stacking *P* and *S* spectra, *J. Geophys. Res*., Vol. 109, No. B08310, doi: 10.1029/2004JB003084.

Sato, T., and T. Hirasawa (1973). Body wave spectra from propagating shear cracks, *J. Phys. Earth*, Vol. 21, pp. 415-431.

Scognamiglio, L. and L. Hutchings (2009). A test of a physically-based strong ground motion prediction methodology with the 27 September 1997, Mw = 6.0 Colfiorito (Umbria-Marcha sequence), Italy earthquake, *Tectonophysics*, Vol. 476, pp. 145-158.

Scholz, C. H. (1982). Scaling laws for large earthquakes: Consequences for physical models, *Bull. Seism. Soc. Am*., Vol. 72, pp. 1-14.

Shearer, P. M., G. A. Prieto, and E. Hauksson (2006). Comprehensive analysis of earthquake source spectra in southern California, *J. Geophys. Res*., Vol. 111, No. B06303, doi: 10.1029/2005JB003979.

Shi, J., W.-Y. Kim, and P. Richards (1998). The corner frequency and stress drops of intraplate earthquakes in the northeastern United States, *Bull. Seism. Soc. Am*., Vol. 88, pp. 531-542.

Somerville, P. G., M. Sen, and B. Cohee (1991). Simulation of strong ground motion recorded during the 1985 Michoacan Mexico and Valparaiso, Chile earthquakes. *Bull. Seism. Soc. Am.,* Vol. 81, pp. 1–28.

Somerville, P., K. Irikura, R. Graves, S. Sawada, D. Wald, N. Abrahamson, Y. Iwasaki, T. Kagawa, N. Smith, and A. Kowada (1999). Characterizing Crustal Earthquake Slip Models for the Prediction of Strong Ground Motion, *Seis. Res. Lett*., Vol. 70, No. 1, pp. 59-80.

Spottiswoode, S. M. and A. McGarr (1975). Source parameters of tremor in a deep-level gold mine, *Bull. Seism. Soc. Am.,* Vol. 65, pp. 93–112.

Spudich, P. and L. N. Frazier (1984). Use of ray theory to calculate high-frequency radiation from earthquake sources having spatially variable rupture velocity and stress drop. *Bull. Seism. Soc. Am*., Vol. 74, pp. 2061-2082.

Steidl, J. H., A. G. Tumarkin and R. J. Archuleta (1996). What is a reference site? *Bull. seism. Soc. Am.,* Vol. 86, pp. 1733–1748.

Tomic, J., R. E. Abercrombie, and A. F. do Nascimento (2009). Source parameters and rupture velocity of small M≤2.1 reservoir induced earthquakes, *Geophys. J. Int.*, doi:10.1111/j.1365-246X.2009.04233.x.

Trifunac, M. D. and J. N. Brune (1970). Complexity of energy release during the Imperial Valley, California, earthquake of 1940, *Bull Seism. Soc. Am.,* Vol. 60, pp. 137-160.

Tumarkin, A.G., R.J. Archuleta, and R. Madariaga (1994). Scaling relations for composite models. *Bull. Seism. Soc. Am.,* Vol. 84, No. 4, pp 1279-1283.

Venkataraman, A., J. Mori, H. Kanamori, and L. Zhu (2000). Fine structure of the rupture zone of the April 26 and 27, 1997, Northridge aftershocks, *J. geophys. Res.,* Vol. 105, pp. 19085–19093.

Viegas, G. (2009). Earthquake Source Properties and Wave Propagation in Eastern North America, *Ph.D. Thesis, Boston University*.

Viegas, G. (2011). Source parameters of the July 16 2010 M3.4 Germantown, MD, Earthquake, *Seism. Res. Lett.,* (in review).

Viegas, G., R. E. Abercrombie, and W.-Y. Kim (2010). The 2002 *M*5 Au Sable Forks, NY, earthquake sequence: Source scaling relationships and energy budget, *J. Geophys. Res.*, Vol. 115, No. B07310, doi: 10.1029/2009JB006799.

Viegas, G., R. E. Abercrombie, and K. Mayeda (2011). Coda derived source parameters in Eastern North America, *Seism. Res. Lett*., (in review).

Wald, D. J., D. V. Helmberger, and T. H. Heaton (1991). Rupture model of the 1989 Loma Prieta earthquake from the inversion of strong-motion and broadband teleseismic data, *Bull. seism. Soc. Am.,* Vol. 81, pp. 1540–1572.

Wald, D. J., and T. H. Heaton (1994). Spatial and temporal distribution of slip for the 1992 Landers, California, earthquake, *Bull. seism. Soc. Am.,* Vol. 84, pp. 668–691.

Wald, D. J., (1995). A preliminary dislocation model for the 1995 Kobe (Hyogo-ken Nanbu), Japan, earthquake determined from strong motion and teleseismic waveforms, *Seism. Res. Lett.,* Vol. 66, pp. 22–28.

Wald, D. J., T. H. Heaton, and K. W. Hudnut (1996). The slip history of the 1994 Northridge, California, earthquake determined from strong-motion, teleseismic, GPS, and leveling data, *Bull. seism. Soc. Am.,* Vol. 86, No. 1, Part B Suppl., pp. 49–70.

Wald, D. J., and R. W. Graves (2001). Resolution Analysis of Finite Fault Source Inversion Using 1D and 3D Green's Functions, Part II: Combining Seismic and Geodetic Data, *J. Geophys. Res*., Vol. 106, No. B5, pp. 8767.

Wells, D. L. and K. J. Coppersmith (1994). New Empirical Relationships among Magnitude, Rupture Length, Rupture Width, Rupture Area, and Surface Displacement. *Bull. Seism. Soc. Am*., Vol. 84, pp. 974-1002.

Wennerberg, L. (1990). Stochastic summation of empirical Green''s functions, *Bull. Seismol. Soc. Am.,* Vol. 80, pp. 1418-1432.

Wossner, J., M. Treml and F. Wenzel (2002). Simulation of Mw = 6.0 earthquakes in the Upper Rhinegraben using empirical Green functions, *Geophys. J. Int*., 151, 487-500.

Wu, F. (1978). Prediction of strong ground motion using small earyhquakes, in *Proceedings of 2nd International Conference on Microzonation Nati. Sci. Found*., San Francisco, Calif., 701-704.

Xie, J., Z. Liu, R. B. Herrmann, and E. Cranswick (1991). Source processes of three aftershocks of the 1983 Goodnow, New York, earthquake: High-resolution images of small, symmetric ruptures, *Bull. Seism. Soc. Am*., Vol. 81, pp. 818-843.

Yamada, T., J. Mori, S. Ide, R. E. Abercrombie, H. Kawakata, M. Nakatani, Y. Iio, and H. Ogasawara (2007). Stress drops and radiated seismic energies of microearthquakes in a South African gold mine, *J. Geophys. Res.*, Vol. 112, No. B03305, doi: 10.1029/2006JB004553.

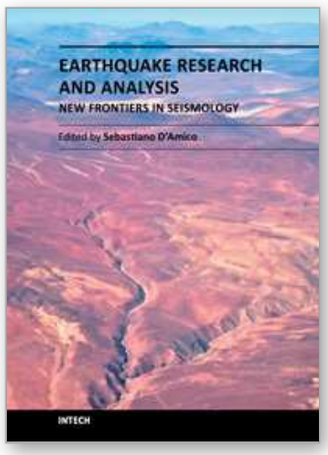

Earthquake Research and Analysis - New Frontiers in Seismology
Edited by Dr Sebastiano D'Amico

ISBN 978-953-307-840-3
Hard cover, 380 pages
Publisher InTech
Published online 27, January, 2012
Published in print edition January, 2012

The study of earthquakes combines science, technology and expertise in infrastructure and engineering in an effort to minimize human and material losses when their occurrence is inevitable. This book is devoted to various aspects of earthquake research and analysis, from theoretical advances to practical applications. Different sections are dedicated to ground motion studies and seismic site characterization, with regard to mitigation of the risk from earthquake and ensuring the safety of the buildings under earthquake loading. The ultimate goal of the book is to encourage discussions and future research to improve hazard assessments, dissemination of earthquake engineering data and, ultimately, the seismic provisions of building codes.

InTech Europe
University Campus STeP Ri
Slavka Krautzeka 83/A
51000 Rijeka, Croatia
Phone: +385 (51) 770 447
Fax: +385 (51) 686 166
www.intechopen.com

InTech China
Unit 405, Office Block, Hotel Equatorial Shanghai
No.65, Yan An Road (West), Shanghai, 200040, China
中国上海市延安西路65号上海国际贵都大饭店办公楼405单元
Phone: +86-21-62489820
Fax: +86-21-62489821

IntechOpen